

Loss-tolerant linear optical quantum computing under nonideal fusions using parity-state-encoded multiphoton qubits

Seok-Hyung Lee,¹ Srikrishna Omkar,² Yong Siah Teo,¹ and Hyunseok Jeong^{1,*}

¹*Department of Physics and Astronomy, Seoul National University, Seoul 08826, Republic of Korea*

²*ORCA Computing, Toronto M6P3T1, Canada*

We propose an all-optical quantum computing protocol using parity-state-encoded multiphoton qubits. It turns out to be highly photon-loss tolerant and resource-efficient even under the effects of nonideal fusions that unavoidably corrupt nearby qubits but have not been rigorously investigated in previous works. For realistic error simulations, we introduce a methodology to analyze such detrimental effects systematically and show that our protocol provides a high photon loss threshold of $\sim 8.5\%$ even with the corrupting effects of nonideal fusions. Further, a logical error rate of 10^{-6} is achieved with $\sim 5 \times 10^5$ three-photon resource states when the photon loss rate is 1%, which outperforms other known linear-optical quantum computing protocols. We also show that previous approaches with single-photon qubits or simple repetition codes are far less efficient than our proposed protocol under lossy environments. Our work not only points out the limitations of existing protocols but also provides a way to overcome them to implement fault-tolerant quantum computing.

Introduction.—Photonic qubits are a promising candidate for quantum computing (QC) with the advantages of long decoherence time, ease of single-qubit manipulation via linear optical circuits, and ease of detecting photon losses by counting photon numbers [1]. A representative way to achieve universal QC in linear optical systems is measurement-based QC (MBQC) [2, 3] processed by single-qubit measurements on a multi-qubit *cluster state*. In particular, a family of cluster states called Raussendorf-Harrington-Goyal (RHG) lattices [4–6] permits universal fault-tolerant QC [7–9], although state distillation [10] is required for non-Clifford gates.

The generation of RHG lattices, which is a significant challenge for realizing fault-tolerant optical MBQC, can be done by entangling multiple small resource states with fusions of type I or II [11]. Both types of fusions are not ideal in linear optics because of theoretical limitations and environmental factors such as photon losses. Fusion success rates cannot exceed 50% without additional resources [12], which is far insufficient to implement MBQC [13]. There exist several types of approaches to overcome this shortcoming. Some examples are (i) different types of encoding strategies with coherent states [14, 15], hybrid qubits [16, 17], and multiphoton qubits [18, 19] that significantly improve error thresholds and resource overheads [19], (ii) ancillary photons to boost the success rate of a type-II fusion to 75% [20, 21], which enables MBQC with the renormalization method [22], (iii) redundant structures added to resource states to replace a single fusion by multiple fusion attempts [23–25], and (iv) use of squeezing for teleportation channels [26] or inline-processes [27, 28].

Previous studies frequently treated fusion failures with edge removals [29–31] or edge-connected qubit removals [13, 16, 19, 22]. However, to accurately evaluate the performance of computing protocols, the detrimental effects of nonideal fusions affecting nearby qubits should be ana-

lyzed more rigorously. In this Letter, we study how nonideal fusions corrupt stabilizers and how errors arising from such corruption are propagated during the generation of cluster states. We show that this effect is equivalent to assigning specific error rates on some qubits in the final lattice, which enables much more realistic error simulations and can be used for decoding syndromes.

We then propose an all-optical fault-tolerant MBQC protocol termed a *parity-state-encoding-based topological quantum computing* (PTQC), which employs the parity-state encoding [32] and concatenated Bell-state measurement (CBSM) [33]. The protocol requires on-off or two-photon resolving detectors, optical switches, delay lines, and three-photon resource states that can be generated with linear optics. We analyze the loss-tolerance and resource overheads of the protocol while exhaustively tracking the detrimental effects of nonideal fusions. In the same way, we also evaluate two other known approaches: one using single-photon qubits with fusions assisted by ancillary photons and the other using simple repetition codes. The former has been widely studied in the context of ballistic QC [22, 29–31], but rigorous error analyses considering both photon losses and nonideal fusions in RHG lattices are missing. For the latter one investigated in our recent work [19], we check how much the rigorous analysis of nonideal fusions varies the obtained results. We verify that both approaches are far less efficient than PTQC.

Preliminaries.—We denote the four Bell states by $|\Phi^\pm\rangle := |0\rangle|0\rangle \pm |1\rangle|1\rangle$ and $|\Psi^\pm\rangle := |0\rangle|1\rangle \pm |1\rangle|0\rangle$ (normalization coefficients are omitted) and call “ \pm ” its *sign* and “ Φ ” or “ Ψ ” its *letter*. An ideal Bell-state measurement (BSM) entails the measurements of $X \otimes X$ and $Z \otimes Z$ on two qubits, whose outcomes are addressed as its sign and letter outcomes, respectively. We use the polarization of photons as the degree of freedom to encode quantum information and denote the horizontally

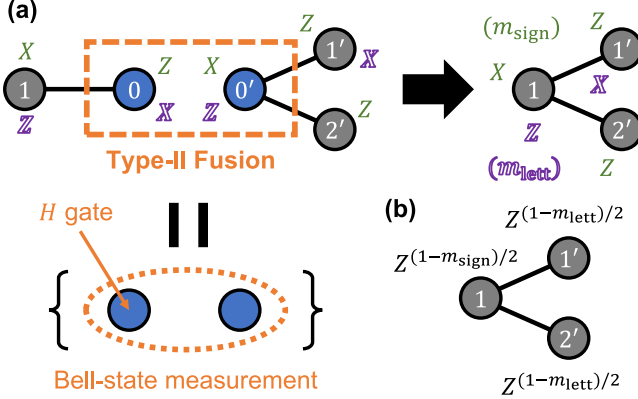


FIG. 1. Example of a type-II fusion done by measuring $Z_0X_{0'}$ and $X_0Z_{0'}$ on the two cluster states. In (a), two stabilizers (green and purple operators) become those of the resulting cluster state up to sign factors (the sign or letter outcome m_{sign} , m_{lett} of the BSM) after the fusion. The final state is the cluster state shown in (b), where the presented Pauli-Z operators are applied.

(vertically) polarized single-photon state by $|\text{H}\rangle$ ($|\text{V}\rangle$).

For a given graph G of qubits, a cluster state $|G\rangle$ is defined as the state stabilized by $S_v := X_v \prod_{v' \in N(v)} Z_{v'}$ (that is, $S_v |G\rangle = |G\rangle$) for each vertex v , where X_v and Z_v are respectively Pauli-X and Z operators on the qubit v and $N(v)$ is the set of the vertices connected with v . Among the two types of fusions, we only consider type II since type I may convert photon losses into unheralded errors [25]. A type-II fusion is done by measuring $X \otimes Z$ and $Z \otimes X$ on two qubits. In practice, it is realized by applying the Hadamard gate on one of the qubits and then performing a BSM on them. For two qubits (v_1, v_2) , if $\{v_1\} \cup N(v_1)$ and $\{v_2\} \cup N(v_2)$ are disjoint, the effect of a fusion on the qubits is to connect (disconnect) every possible pair of disconnected (connected) qubits, one from $N(v_1)$ and the other from $N(v_2)$, up to several Pauli-Z operators determined by the BSM outcome. These Pauli-Z operators are compensated by updating the Pauli frame [34] classically. This effect can be checked by tracking the transformation of stabilizers, as shown in the example of Fig. 1.

We consider errors of qubits in the “vacuum” [4] measured in the X -basis; thus, X -errors do not affect the results. Henceforth, every error mentioned is a Z -error.

Nonideal fusions.—Let us consider the example of Fig. 1, supposing that the qubits are single-photon polarization ones. Then the BSM can discriminate only two Bell states (say, $|\Phi^\pm\rangle$) among the four without additional resources [35]. The intact final state $|C_f\rangle$ is obtained only when the BSM succeeds. When the BSM fails (which is heralded), m_{lett} is determined while m_{sign} is left ambiguous. We randomly assign the value of m_{sign} since the marginal state of qubits 0 and 0' is maximally mixed be-

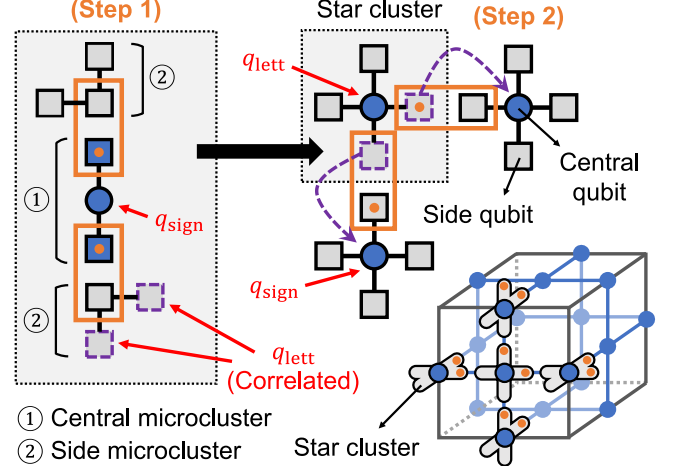


FIG. 2. Lattice building process with microclusters. The orange boxes indicate fusions, where the locations of the Hadamard gates (orange dots) are determined under the H -configuration of HIC. In step 1, side and central microclusters are fused to form a star cluster. In step 2, multiple star clusters are fused to form an RHG lattice. The macroscopic picture of step 2 in a unit cell of an RHG lattice is depicted in the lower right. The error probabilities of qubits assigned by one fusion in each step are written in red, where q_{sign} (q_{lett}) is the sign (letter) probability of the BSM. Errors in the side qubits remaining after step 1 (purple dashed squares) are propagated to central qubits during step 2 (purple dashed arrows).

fore the fusion [36]. Then, the operator $m_{\text{sign}}X_1Z_{1'}Z_{2'}$, which is a stabilizer of $|C_f\rangle$, gives ± 1 randomly when it is measured on the real final state. Whereas, the other two stabilizers $m_{\text{lett}}Z_1X_{1'}$ and $m_{\text{lett}}Z_1X_{2'}$ are left undamaged. The key point is that this situation is equivalent to a 50% chance of an erroneous qubit 1 in $|C_f\rangle$ in terms of stabilizer statistics. In other words, both situations give the same statistics if the stabilizers of $|C_f\rangle$ are measured; thus, every process in MBQC described with the stabilizer formalism works in the same way.

Generally, a nonideal BSM gives one of the possible outcomes, and a Bell state that gives the highest posterior probability under the outcome is selected, assuming that the four Bell states have the same prior probability. From the posterior probabilities, the probability q_{sign} (q_{lett}) that the selected sign (letter) is wrong is obtained. Then, in the case of Fig. 1, this is equivalent to qubit 1 having an error with probability q_{sign} and qubits 1' and 2' having correlated errors with probability q_{lett} . We term a qubit with a nonzero error rate *deficient*. Additionally, if a qubit participated in a fusion is erroneous, this error is propagated to the qubits on the opposite side. For example, an erroneous qubit 0 induces an error in the $X_0Z_{0'}$ measurement, which is equivalent to erroneous qubits 1' and 2'.

Building a lattice.—An RHG lattice can be built with two types of linear three-qubit cluster states called *cen-*

tral and side microclusters [22, 29]. The process is composed of two steps (see Fig. 2): In step 1, a central microcluster and two side microclusters are merged by two fusions to form a five-qubit *star cluster* composed of a *central qubit* and four *side qubits*. In step 2, the side qubits of star clusters are fused to form an RHG lattice. Eventually, the lattice includes only the central qubits, measured in appropriate bases for MBQC. For step 2, we consider two options: (i) Star clusters with successful step-1 fusions may be post-selected, or (ii) all generated star clusters are used regardless of the fusion results. The locations of Hadamard gates during fusions (called *H-configuration*) may be chosen arbitrarily. Here, we define two specific configurations: *HIC* and *HIS*. In *HIC* (*HIS*), the Hadamard gates in step 1 are applied on qubits in the central (side) microclusters. Whereas the Hadamard gates in step 2 are arranged in the same pattern for both configurations as shown in Fig. 2.

Nonideal fusions during lattice building render some qubits deficient, as shown in Fig. 2 when *HIC* is used. (When *HIS* is used, the positions of q_{sign} and q_{lett} in the figure are swapped.) Note that errors in the side qubits, if any, are propagated to the nearest central qubits after step 2. Correlation between the sign and letter errors of a fusion, if any, can be neglected if the primal and dual lattices are considered separately, since these errors respectively affect primal and dual [4] qubits (or vice versa).

Noise model.—We consider a noise model where each photon suffers an independent loss with probability η , which arises from imperfections throughout the protocol: three-photon Greenberger-Horne-Zeilinger (GHZ-3) states (which are initial resource states), delay lines, optical switches, and photodetectors. We assume that noise that cannot be modeled with photon losses such as dark counts is negligible. Note that photon losses in central qubits, which are detectable by on-off detectors, also incur deficiency. If the measurement outcome of a center qubit cannot be determined due to photon losses, we select the outcome randomly and assign an error rate of 50% to the qubit.

PTQC protocol.—We introduce the new PTQC protocol, where fusion success rates are boosted by using the parity-state encoding [32] for all qubits except central ones (which are single-photon polarization qubits) and employing CBSM [33]. On-off or two-photon resolving detectors are used as photodetectors, and all resource states can be generated linear-optically. The (n, m) parity-state encoding defines a basis as $|0_L\rangle := |+(^m)\rangle^{\otimes n}$ and $|1_L\rangle := |-(^m)\rangle^{\otimes n}$, where $|\pm(^m)\rangle := (|H\rangle + |V\rangle)^{\otimes m} \pm (|H\rangle - |V\rangle)^{\otimes m}$. The Hilbert space has a hierarchical structure composed of three levels: the lattice, block, and physical levels with respective bases $\{|0_L\rangle, |1_L\rangle\}$, $\{|\pm(^m)\rangle\}$, and $\{|H\rangle, |V\rangle\}$. In the original CBSM scheme [33], a BSM of a certain level is decomposed into multi-

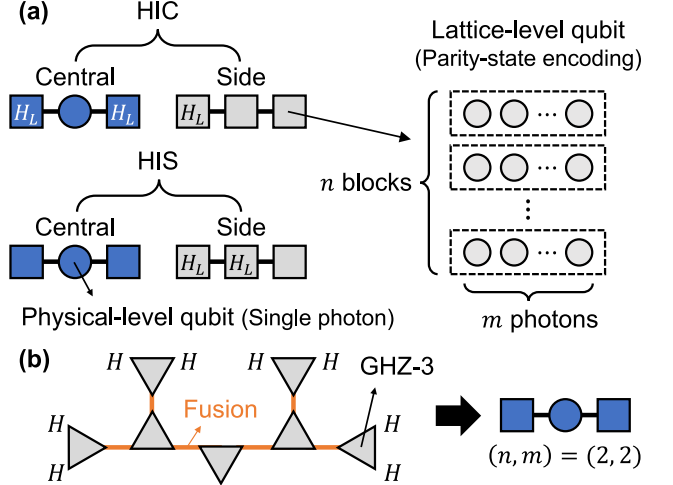


FIG. 3. (a) Schematic of the central and side post- H microclusters used in PTQC for the two H -configurations, *HIC* and *HIS*. The marks “ H_L ” indicate the locations of the lattice-level Hadamard gates. (b) Example of a process generating a post- H microcluster from GHZ-3 states. Each GHZ-3 state is represented by a triangle whose vertices indicate its three photons. An orange line connecting two vertices and a mark “ H ” next to a vertex respectively mean a fusion and Hadamard gate performed on the photon(s).

ple BSMs of one level below. Our current CBSM scheme slightly differs from the original one in the following two areas: (i) We consider two types of photodetectors: two-photon resolving and on-off detectors. A physical-level BSM can discriminate between a photon loss and failure only if two-photon resolving detectors are used. (ii) The letter outcome of a lattice-level BSM is obtained by a weighted majority vote of block-level letter outcomes. See Secs. II and III of [36] for details of the CBSM scheme and its error rates, respectively.

For practical reasons, we consider generating *post-H* microclusters (that is, the states obtained by applying several lattice-level Hadamard gates on microclusters) directly, instead of generating microclusters first and then applying the Hadamard gates for the fusions. Figure 3(a) depicts the central and side post- H microclusters for *HIC* and *HIS*, which are generated by fusing multiple GHZ-3 states appropriately, as shown in the example of Fig. 3(b). See Sec. V of [36] for details of the structures of post- H microclusters and their generation.

The resource overhead of PTQC is quantified by the expected total number N_{p_L} of GHZ-3 states to achieve a target logical error rate of p_L , which depends on η , for the logical identity gate of $T = d - 1$. The process of generating a post- H microcluster should be fine-tuned to minimize the resource overhead. In particular, it is severely affected by the order of the BSMs in the process since we take a strategy of discarding all photons that are entangled with the photons involved in failed BSMs

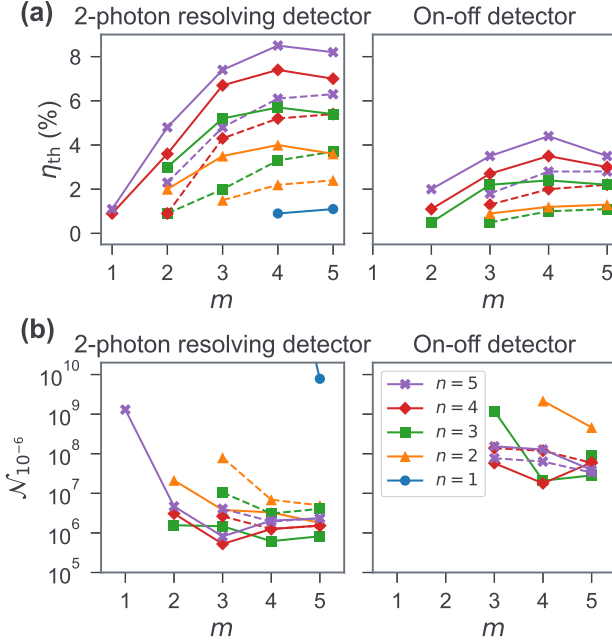


FIG. 4. (a) Photon loss thresholds η_{th} and (b) resource overheads $N_{10^{-6}}$ at $\eta = 1\%$ as functions of n and m for the two types of photodetectors. The solid (dashed) lines are from the protocol with (without) the post-selection of star clusters. Each data point is optimized between HIC and HIS.

to ensure that the final post- H microcluster is generated without failed BSMs. See Sec. VI of [36] for details of the fine-tuning problem.

For error simulations, we consider the logical identity gate with the length T of $4d + 1$ unit cells along the simulated time axis, where d is the code distance. All the fusion outcomes are sampled from appropriate probability distributions, and the corresponding error rates are assigned to individual central qubits according to the process described earlier. These error rates are exploited when decoding syndromes by the *weighted* minimum-weight perfect matching decoder in the Py-Matching package [37]. The loss thresholds are calculated by finding the intersections of logical error rates for $d = 9$ and $d = 11$. See Sec. VII of [36] for the details of the simulation method.

The simulation results of the loss thresholds and resource overheads are presented in Fig. 4 for the two types of photodetectors and the two options for the post-selection of star clusters. Figure 4(a) shows that, when two-photon resolving (on-off) detectors are used, η_{th} reaches up to 8.5% (4.4%) when $n = 5$, $m = 4$, and star clusters are post-selected. The post-selection increases the photon loss threshold by up to $\sim 2\%$ ($\sim 1\%$) when two-photon resolving (on-off) detectors are used. From Fig. 4(b), it is observed that the protocol using two-photon resolving (on-off) detectors is most

resource-efficient with $N_{10^{-6}} \approx 5 \times 10^5$ (6×10^6) when $n = 4$, $m = 3$ ($n = m = 4$), HIC (HIS) is used, and star clusters are post-selected. More detailed simulation results are shown in Sec. VIII of [36], which includes differences between the two H -configurations, the numbers of required GHZ-3 states per central qubit, and the list of optimal parameter settings.

Analyses of other approaches.—We evaluate the performance of two other known approaches, one using single photons for all qubits with fusions assisted by ancillary photons and the other using repetition codes, with the introduced methodology for analyzing nonideal fusions; see Sec. IX of [36] for detailed methods and results. It is observed that PTQC is far more efficient than these two approaches.

For the former approach, which has been studied widely in the literature [22, 29–31], our simulation shows that the fusion failure rate should be less than about 10% even if η is only 1%. To achieve such a low failure rate, accurate photon-number resolving detectors (PNRDs) resolving up to 16 photons and ancillary eight-photon entangled states hard to generate with linear optics are required [21], which is highly difficult to implement. Moreover, our simulation does not consider the imperfection of ancillary states and additional PNRDs; if they are considered, the requirements will be even stricter. However, we note that there is a possibility that the lattice renormalization method in [22] may make the protocol less demanding, which is worth investigating in future works.

For the approach with repetition codes [19], it is observed that the recalculated photon loss thresholds are lower than the values reported in [19], which shows that PTQC is much more loss-tolerant than this approach. For example, if each central qubit consists of two photons, the obtained optimal photon loss threshold is 0.97% (0.40%) when star clusters are (are not) post-selected, while the reported value is 3.3% (3.1%). Moreover, encoding central qubits with the repetition code does not improve the performance significantly [36].

Discussion.—We investigate the detrimental effects of nonideal type-II fusions on the qubits in cluster states used for linear optical topological measurement-based quantum computing (MBQC). With this methodology, we show that our proposed parity-state-encoding-based topological quantum computing (PTQC) protocol that employs the parity-state encoding and concatenated Bell-state measurement permits high loss thresholds of around 8.5%. Moreover, logical error rates near 10^{-6} can be achieved using about 10^6 or fewer GHZ-3 states in total when the photon loss rate is 1%, which outperforms other known linear optical computing protocols [19]. We also investigate two other known approaches that respectively use single-photon qubits with fusions assisted by ancillary photons and repetition codes. We verify that they are highly demanding compared to PTQC due to low photon loss thresholds or hard-to-implement requirements

such as photodetectors that can resolve many photons. Therefore, PTQC is competitive for near-term universal fault-tolerant linear optical quantum computing.

One may apply our method of analyzing nonideal fusions to other encoding schemes or decoding algorithms (such as the union-find decoder [38]) to improve fault-tolerance or resource overheads. More careful consideration of component-wise errors, including both heralded photon losses and unheralded errors (such as dark counts on photodetectors), shall give rise to more realistic analyses. Lastly, our methods may be generalized to fusion-based quantum computing [39] that is attracting attention recently, or other MBQC protocols such as the color-code-based one [40].

* jeongh@snu.ac.kr

[1] T. C. Ralph and G. J. Pryde, Chapter 4 - Optical Quantum Computation (Elsevier, 2010) pp. 209–269.

[2] R. Raussendorf and H. J. Briegel, A one-way quantum computer, *Phys. Rev. Lett.* **86**, 5188 (2001).

[3] R. Raussendorf, D. E. Browne, and H. J. Briegel, Measurement-based quantum computation on cluster states, *Phys. Rev. A* **68**, 022312 (2003).

[4] R. Raussendorf, J. Harrington, and K. Goyal, A fault-tolerant one-way quantum computer, *Ann. Phys.* **321**, 2242 (2006).

[5] R. Raussendorf, J. Harrington, and K. Goyal, Topological fault-tolerance in cluster state quantum computation, *New J. Phys.* **9**, 199 (2007).

[6] A. G. Fowler and K. Goyal, Topological cluster state quantum computing, *Quantum Info. Comput.* **9**, 721–738 (2009).

[7] D. Herr, A. Paler, S. J. Devitt, and F. Nori, Lattice surgery on the Raussendorf lattice, *Quantum Sci. Technol.* **3**, 035011 (2018).

[8] B. J. Brown and S. Roberts, Universal fault-tolerant measurement-based quantum computation, *Phys. Rev. Research* **2**, 033305 (2020).

[9] H. Bombin, C. Dawson, R. V. Mishmash, N. Nickerson, F. Pastawski, and S. Roberts, Logical blocks for fault-tolerant topological quantum computation, arXiv preprint arXiv:2112.12160 (2021).

[10] S. Bravyi and A. Kitaev, Universal quantum computation with ideal Clifford gates and noisy ancillas, *Phys. Rev. A* **71**, 022316 (2005).

[11] D. E. Browne and T. Rudolph, Resource-efficient linear optical quantum computation, *Phys. Rev. Lett.* **95**, 010501 (2005).

[12] S. L. Braunstein and A. Mann, Measurement of the Bell operator and quantum teleportation, *Phys. Rev. A* **51**, R1727 (1995).

[13] J. M. Auger, H. Anwar, M. Gimeno-Segovia, T. M. Stace, and D. E. Browne, Fault-tolerant quantum computation with nondeterministic entangling gates, *Phys. Rev. A* **97**, 030301(R) (2018).

[14] H. Jeong, M. S. Kim, and J. Lee, Quantum-information processing for a coherent superposition state via a mixedentangled coherent channel, *Phys. Rev. A* **64**, 052308 (2001).

[15] H. Jeong and M. S. Kim, Efficient quantum computation using coherent states, *Phys. Rev. A* **65**, 042305 (2002).

[16] S. Omkar, Y. S. Teo, and H. Jeong, Resource-efficient topological fault-tolerant quantum computation with hybrid entanglement of light, *Phys. Rev. Lett.* **125**, 060501 (2020).

[17] S. Omkar, Y. S. Teo, S.-W. Lee, and H. Jeong, Highly photon-loss-tolerant quantum computing using hybrid qubits, *Phys. Rev. A* **103**, 032602 (2021).

[18] S.-W. Lee, K. Park, T. C. Ralph, and H. Jeong, Nearly deterministic bell measurement with multiphoton entanglement for efficient quantum-information processing, *Phys. Rev. A* **92**, 052324 (2015).

[19] S. Omkar, S.-H. Lee, Y. S. Teo, S.-W. Lee, and H. Jeong, All-photonic architecture for scalable quantum computing with greenberger-horne-zeilinger states, *PRX Quantum* **3**, 030309 (2022).

[20] W. P. Grice, Arbitrarily complete Bell-state measurement using only linear optical elements, *Phys. Rev. A* **84**, 042331 (2011).

[21] F. Ewert and P. van Loock, 3/4-Efficient Bell measurement with passive linear optics and unentangled ancillae, *Phys. Rev. Lett.* **113**, 140403 (2014).

[22] D. Herr, A. Paler, S. J. Devitt, and F. Nori, A local and scalable lattice renormalization method for ballistic quantum computation, *npj Quantum Information* **4**, 1 (2018).

[23] K. Fujii and Y. Tokunaga, Fault-tolerant topological one-way quantum computation with probabilistic two-qubit gates, *Phys. Rev. Lett.* **105**, 250503 (2010).

[24] Y. Li, S. D. Barrett, T. M. Stace, and S. C. Benjamin, Fault tolerant quantum computation with nondeterministic gates, *Phys. Rev. Lett.* **105**, 250502 (2010).

[25] Y. Li, P. C. Humphreys, G. J. Mendoza, and S. C. Benjamin, Resource costs for fault-tolerant linear optical quantum computing, *Phys. Rev. X* **5**, 041007 (2015).

[26] S. Takeda, T. Mizuta, M. Fuwa, P. Van Loock, and A. Furusawa, Deterministic quantum teleportation of photonic quantum bits by a hybrid technique, *Nature* **500**, 315 (2013).

[27] H. A. Zaidi and P. van Loock, Beating the one-half limit of ancilla-free linear optics Bell measurements, *Phys. Rev. Lett.* **110**, 260501 (2013).

[28] T. Kilmer and S. Guha, Boosting linear-optical bell measurement success probability with predetection squeezing and imperfect photon-number-resolving detectors, *Phys. Rev. A* **99**, 032302 (2019).

[29] M. Gimeno-Segovia, P. Shadbolt, D. E. Browne, and T. Rudolph, From three-photon Greenberger-Horne-Zeilinger states to ballistic universal quantum computation, *Phys. Rev. Lett.* **115**, 020502 (2015).

[30] H. A. Zaidi, C. Dawson, P. van Loock, and T. Rudolph, Near-deterministic creation of universal cluster states with probabilistic Bell measurements and three-qubit resource states, *Phys. Rev. A* **91**, 042301 (2015).

[31] M. Pant, D. Towsley, D. Englund, and S. Guha, Percolation thresholds for photonic quantum computing, *Nat. Commun.* **10**, 1 (2019).

[32] T. C. Ralph, A. J. F. Hayes, and A. Gilchrist, Loss-tolerant optical qubits, *Phys. Rev. Lett.* **95**, 100501 (2005).

[33] S.-W. Lee, T. C. Ralph, and H. Jeong, Fundamental building block for all-optical scalable quantum networks,

Phys. Rev. A **100**, 052303 (2019).

[34] E. Knill, Quantum computing with realistically noisy devices, *Nature* **434**, 39 (2005).

[35] N. Lütkenhaus, J. Calsamiglia, and K.-A. Suominen, Bell measurements for teleportation, *Phys. Rev. A* **59**, 3295 (1999).

[36] See the Supplemental Material for details of methods, discussions, proofs, and calculations.

[37] O. Higgott, Pymatching: A python package for decoding quantum codes with minimum-weight perfect matching, *ACM Trans. Quantum Comput.* 10.1145/3505637 (2021).

[38] N. Delfosse and N. H. Nickerson, Almost-linear time decoding algorithm for topological codes, *Quantum* **5**, 595 (2021).

[39] S. Bartolucci, P. Birchall, H. Bombin, H. Cable, C. Dawson, M. Gimeno-Segovia, E. Johnston, K. Kieling, N. Nickerson, M. Pant, *et al.*, Fusion-based quantum computation, arXiv preprint arXiv:2101.09310 (2021).

[40] S.-H. Lee and H. Jeong, Universal hardware-efficient topological measurement-based quantum computation via color-code-based cluster states, *Phys. Rev. Research* **4**, 013010 (2022).

Supplemental Material

Loss-tolerant linear optical quantum computing under nonideal fusions using parity-state-encoded multiphoton qubits

Seok-Hyung Lee,¹ Srikrishna Omkar,² Yong Siah Teo,¹ and Hyunseok Jeong^{1,*}

¹*Department of Physics and Astronomy, Seoul National University, Seoul 08826, Republic of Korea*

²*ORCA Computing, Toronto M6P3T1, Canada*

I. PROOF OF THE STATEMENT ON MARGINAL STATES OF A CLUSTER STATE

We here prove the statement: *For a cluster state $|G\rangle_V$ with a graph $G = (V, E)$ and given two vertices $a, b \in V$, if $\{a\} \cup N(a)$ and $\{b\} \cup N(b)$ are disjoint and neither $N(a)$ nor $N(b)$ is empty where $N(v)$ for a vertex $v \in V$ is the set of vertices adjacent to v , the marginal state $\text{Tr}_{V \setminus \{a, b\}} |G\rangle \langle G|_V =: \rho_{ab}$ is maximally mixed.*

Let \mathcal{S} denote the stabilizer group of the zero-dimensional Hilbert space $\{|G\rangle_V\}$. First, any stabilizer $S \in \mathcal{S}$ can be written as the product of stabilizer generators: $S = \prod_{v \in V_0} S_v$ where $V_0 \subseteq V$ and $S_v := X_v \prod_{v' \in N(v)} Z_{v'}$. If V_0 contains a vertex $c \neq a, b$, S must contain X_c or Y_c since no stabilizer generators besides S_c contain X_c . If otherwise, V_0 is one of \emptyset , $\{a\}$, $\{b\}$, and $\{a, b\}$. Except when V_0 is empty (namely, S is identity), there exists a vertex $c \neq a, b$ such that S contains Z_c , since $N(a)$ and $N(b)$ are not empty, $b \notin N(a)$, $a \notin N(b)$, and $N(a) \neq N(b)$. Therefore, every single- or two-qubit Pauli operator on a and b that is not identity cannot be a stabilizer, thus it anticommutes with at least one stabilizer. (If such an operator $P_a P_b$ commutes with all stabilizers, $P_a P_b |G\rangle_V$ is also stabilized by \mathcal{S} , which means that $P_a P_b |G\rangle_V = |G\rangle_V$ since \mathcal{S} stabilizes the zero-dimensional Hilbert space.) Consequently, $\text{Tr}(P_a P_b \rho_{ab}) = \langle G | P_a P_b | G \rangle = 0$ for every single- or two-qubit Pauli operator $P_a P_b$ that is not identity. The state ρ_{ab} satisfying this condition is unique and maximally mixed.

II. CONCATENATED BSM SCHEME OF THE PARITY-STATE ENCODING

The (n, m) parity-state encoding defines a basis as $|0_L\rangle := |+^{(m)}\rangle^{\otimes n}$ and $|1_L\rangle := |-(m)\rangle^{\otimes n}$, where $|\pm^{(m)}\rangle := (|H\rangle + |V\rangle)^{\otimes m} \pm (|H\rangle - |V\rangle)^{\otimes m}$. The bases of lattice-, block-, and physical-level Hilbert spaces are respectively given as $\{|0_L\rangle, |1_L\rangle\}$, $\{|\pm^{(m)}\rangle\}$, and $\{|H\rangle, |V\rangle\}$. With the above bases, the sets of the Bell states are respectively defined as $\{|\Phi^\pm\rangle, |\Psi^\pm\rangle\}$, $\{|\phi_{(m)}^\pm\rangle, |\psi_{(m)}^\pm\rangle\}$, and $\{|\phi^\pm\rangle, |\psi^\pm\rangle\}$ for the three levels, where their signs and letters are determined by the same way shown in the main text. For example, $|\Phi^\pm\rangle := |0_L\rangle |0_L\rangle \pm |1_L\rangle |1_L\rangle$ and $|\Psi^\pm\rangle := |0_L\rangle |1_L\rangle \pm |1_L\rangle |0_L\rangle$.

The Bell states of each level can be decomposed into those of one level below as follows:

$$|\Phi^\pm\rangle = 2^{-\frac{n-1}{2}} \sum_{l: \text{even}(\text{odd}) \leq n} \mathcal{P} \left[\left| \phi_{(m)}^- \right\rangle^{\otimes l} \left| \phi_{(m)}^+ \right\rangle^{\otimes n-l} \right], \quad (1a)$$

$$|\Psi^\pm\rangle = 2^{-\frac{n-1}{2}} \sum_{l: \text{even}(\text{odd}) \leq n} \mathcal{P} \left[\left| \psi_{(m)}^- \right\rangle^{\otimes l} \left| \psi_{(m)}^+ \right\rangle^{\otimes n-l} \right], \quad (1b)$$

$$|\phi_{(m)}^\pm\rangle = 2^{-\frac{m-1}{2}} \sum_{k: \text{even} \leq m} \mathcal{P} \left[\left| \psi^\pm \right\rangle^{\otimes k} \left| \phi^\pm \right\rangle^{\otimes m-k} \right], \quad (1c)$$

$$|\psi_{(m)}^\pm\rangle = 2^{-\frac{m-1}{2}} \sum_{k: \text{odd} \leq m} \mathcal{P} \left[\left| \psi^\pm \right\rangle^{\otimes k} \left| \phi^\pm \right\rangle^{\otimes m-k} \right], \quad (1d)$$

where $\mathcal{P}[\cdot]$ means the summation of all the permutations of the tensor products inside the bracket. Therefore, a BSM can be performed in a concatenated manner: A lattice-level BSM (BSM_{lat}) is done by n block-level BSMs (BSM_{blk} 's), each of which is again done by m physical-level BSMs (BSM_{phy} 's). We refer to the sign (letter) result obtained from a lattice-, block-, or physical-level BSM as a lattice-, block-, or physical-level sign (letter), respectively.

* jeongh@snu.ac.kr

A. Original scheme

We first review the original CBSM scheme of the parity-state encoding in Ref. [1]. A BSM_{phy} can discriminate only two among the four Bell states. Three types of BSM_{phy} 's (B_ψ , B_+ , and B_-) are considered, which discriminate $\{|\psi^+\rangle, |\psi^-\rangle\}$, $\{|\phi^+\rangle, |\psi^+\rangle\}$, and $\{|\phi^-\rangle, |\psi^-\rangle\}$, respectively. A BSM_{phy} has four possible outcomes: two successful cases (e.g. , for B_ψ , $|\psi^+\rangle$ and $|\psi^-\rangle$), “failure,” and “detecting a photon loss.” The BSM scheme for single-photon polarization qubits [2] is presented in Fig. 1. Failure and loss are discriminated by the number of total photons detected by the photon detectors. Since two photons may enter a single detector, it is assumed that two-photon resolving detectors (namely, photon-number resolving detectors resolving up to two photons) are used. Note that, even in the failure cases, either sign or letter still can be determined definitely. (For example, even if a B_ψ fails, we can still learn that the letter is ϕ .) On the other hand, if it detects a loss, we can get neither a sign nor a letter. We also note that the failure case contains many combinations of detector outcomes and each of them may individually give some information on the input state. However, we suppose that we forget the exact combination and only know that it fails.

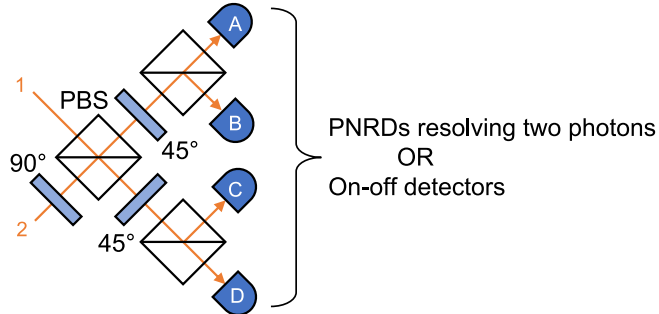


FIG. 1. BSM scheme for single-photon polarization qubits using three polarizing Beam splitters (PBSs), 90° and 45° wave plates, and four (A–D) photon detectors (two-photon resolving or on-off detectors). A PBS transmits (reflects) photons polarized horizontally (vertically). The scheme distinguishes $|\psi^\pm\rangle$: $|\psi^+\rangle$ if detectors (A, C) or (B, D) detect one photon respectively and $|\psi^-\rangle$ if detectors (A, D) or (B, C) detect one photon respectively. If otherwise, it fails or detects a loss, which can be discriminated by the total number of detected photons if two-photon resolving detectors are used. Two distinguishable Bell states can be chosen by putting or removing 90° wave plates appropriately before the first PBS.

A BSM_{blc} is done by m -times of BSM_{phy} 's. Each block is composed of m photons, thus we consider m pairs of photons selected respectively in the two blocks. First, B_ψ is performed on each of such pairs in order until it either succeeds, detects a loss, or consecutively fails j times, where $j \leq m-1$ is a predetermined number. Then a sign $s = \pm$ is selected by the sign of the last B_ψ outcome if it succeeds and randomly if it fails or detects a loss. After that, B_s 's are performed for all the left pairs of photons.

The block-level sign (letter) is determined by the physical-level signs (letters) of the m BSM_{phy} 's. In detail, the block-level sign is chosen (i) to be the same as s if the last B_ψ succeeds or any B_s succeeds, and (ii) to be the opposite of s if the last B_ψ does not succeed and any B_s fails. (iii) Otherwise (namely, if the last B_ψ does not succeed and all the B_s 's detect losses), the block-level sign is not determined. The block-level letter is determined only when all the physical-level letters are determined, namely, when no losses are detected and all B_s 's succeed. For such cases, the block-level letter is ϕ (ψ) if the number of ψ in the BSM_{phy} results is even (odd).

Next, a BSM_{lat} is done by n -times of BSM_{blc} 's. The lattice-level sign is determined only when all the block-level signs are determined; it is (+) if the number of (–) in the BSM_{blc} results is even and it is (–) if the number is odd. The lattice-level letter is equal to any determined block-level letter. Thus, if all BSM_{blc} 's cannot determine letters, the lattice-level letter is not determined as well.

B. Modified scheme for PTQC

In our PTQC protocol, we also consider using on-off detectors instead of two-photon resolving detectors. The CBSM scheme should be slightly modified for this case.

Since failure and loss cannot be discriminated, a BSM_{phy} now has three possible outcomes: two successful cases and failure. Consequently, in a BSM_{blc} , B_ψ 's are performed until it either succeeds or consecutively fails j times. The way to determine the block-level sign and letter is the same as the original scheme, except that case (iii) when

determining the sign no longer occurs. The biggest difference from the original scheme is that the determined sign and letter may be wrong. We explicitly calculate these error probabilities in Sec. III.

In a BSM_{lat} , the lattice-level sign is determined from the block-level signs by the same method as the original scheme, although it may be wrong with a nonzero probability as well. On the other hand, the lattice-level letter is not determined by a single block-level letter as the original scheme; instead, we use a weighted majority vote of block-level letters. The weight of each block-level letter is given as $w := \log [(1 - q_{\text{lett}}^{\text{blc}})/q_{\text{lett}}^{\text{blc}}]$, where $q_{\text{lett}}^{\text{blc}}$ is the probability that the block-level letter is wrong. This weight factor is justified as follows: Let I_ϕ (I_ψ) denote the set of the indices of block pairs where the block-level letters are ϕ (ψ). Assuming that the two lattice-level letters (Φ and Ψ) have the same prior probability, we get

$$\begin{aligned} \frac{\Pr(\Phi|I_\phi, I_\psi)}{\Pr(\Psi|I_\phi, I_\psi)} &= \frac{\Pr(I_\phi, I_\psi|\Phi)\Pr(\Phi)}{\Pr(I_\phi, I_\psi|\Psi)\Pr(\Psi)} = \frac{\Pr(I_\phi, I_\psi|\Phi)}{\Pr(I_\phi, I_\psi|\Psi)} = \frac{\prod_{i \in I_\phi} (1 - q_{\text{lett}}^{(i)}) \prod_{i \in I_\psi} q_{\text{lett}}^{(i)}}{\prod_{i \in I_\phi} q_{\text{lett}}^{(i)} \prod_{i \in I_\psi} (1 - q_{\text{lett}}^{(i)})} \\ &= \prod_{i \in I_\phi} \frac{1 - q_{\text{lett}}^{(i)}}{q_{\text{lett}}^{(i)}} \Bigg/ \prod_{i \in I_\psi} \frac{1 - q_{\text{lett}}^{(i)}}{q_{\text{lett}}^{(i)}} = \exp \left(\sum_{i=1}^n w^{(i)} \right), \end{aligned}$$

where $q_{\text{lett}}^{(i)}$ and $w^{(i)}$ are respectively the letter error probability and the weight of the i th block. Note that the third equality comes from the fact that a lattice-level Bell state is decomposed into block-level Bell states of the same letter, as shown in Eqs. (1a) and (1b).

III. ERROR PROBABILITIES OF A BSM OF PARITY-STATE QUBITS UNDER A LOSSY ENVIRONMENT

We here derive the error probabilities of a BSM on two qubits (say, qubits 1 and 2) encoded with the parity-state encoding. We suppose the loss model in the main text with the photon loss probability η and denote $x := (1 - \eta)^2$, which is the probability that a BSM_{phy} does not detect photon losses. We also assume that the initial marginal state on qubits 1 and 2 before suffering losses is the equal mixture of four lattice-level Bell states. In other words, the four Bell states have the same prior probabilities. We separately consider the scheme using two-photon resolving detectors and that using on-off detectors.

Note that a BSM_{phy} has four possible outcomes (two successful cases, failure, and detecting a loss), and the outcome “detecting a loss” does not occur if on-off detectors are used. For a BSM_{blc} or BSM_{lat} , to avoid confusion, we use the term “outcome” to indicate the tuple of the outcomes of the BSM_{phy} ’s constituting the BSM_{blc} or BSM_{lat} , and use the term “result” to indicate one of the four Bell states that gives the largest posterior probability under its outcome. Note that the result of a BSM may be not deterministically determined by its outcome; if multiple Bell states have the same posterior probability, one of them is randomly selected as the result.

A. With two-photon resolving detectors

The scheme using two-photon resolving detectors is already well explained in Ref. [1]. We here review the contents to be self-contained.

1. Block-level BSM (BSM_{blc})

Considering the determination of a block-level sign and letter in Sec. II A, the outcome of a BSM_{blc} is included in one of the following three cases: (Success) Both the sign and letter are identified if no losses are detected and all the B_\pm ’s succeed. (Failure) Neither sign nor letter is identified if no B_ψ ’s succeed and all B_\pm ’s detect losses. (Sign discrimination) Only the sign is identified if otherwise. The block-level sign (or letter) is selected randomly if it is not identified. The probabilities of these cases are respectively

$$p_s = \left[1 - 2^{-(j+1)} \right] x^m, \quad p_f = \sum_{l=0}^j \left(\frac{x}{2} \right)^l (1 - x)^{m-l}, \quad p_{sd} = 1 - p_s - p_f. \quad (2)$$

2. Lattice-level BSM (BSM_{lat})

For a BSM_{lat} , let N_s (N_f) denote the number of successful (failed) BSM_{blc} 's. The lattice-level letter is identified if $N_s \geq 1$ (namely, if at least one block-level letter is identified) and the sign is identified if $N_f = 0$ (namely, if all block-level signs are identified). Hence, the outcome of a BSM_{lat} is included in one of the following four events:

$$\begin{cases} S \text{ (Success)} : & N_s \geq 1 \wedge N_f = 0, \\ D_L \text{ (Letter discrimination)} : & N_s, N_f \geq 1, \\ D_S \text{ (Sign discrimination)} : & N_s = N_f = 0, \\ F \text{ (Failure)} : & N_s = 0 \wedge N_f \geq 1. \end{cases} \quad (3)$$

The sign and letter error probabilities ($q_{\text{sign}}, q_{\text{lett}}$) of the BSM_{lat} for each event are $(0, 0)$ for S , $(1/2, 0)$ for D_L , $(0, 1/2)$ for D_S , and $(1/2, 1/2)$ for F . The probabilities of the events are respectively given as

$$\begin{aligned} P_S &= (1 - p_f)^n - p_{\text{sd}}^n, \\ P_{D_L} &= 1 - (1 - p_s)^n + (1 - p_f)^n - p_{\text{sd}}^n, \\ P_{D_S} &= p_{\text{sd}}^n, \\ P_F &= (1 - p_s)^n - p_{\text{sd}}^n. \end{aligned} \quad (4)$$

B. With on-off detectors

Next, we investigate the CBSM scheme using on-off detectors; namely, a photon loss in a BSM_{phy} is not detected and just leads to its failure.

1. Block-level BSM (BSM_1)

Each outcome of a BSM_{blc} is uniquely identified by a triple $O = (r, s, \mathbf{U})$, where $r \in \mathbb{Z}_{j+1} := \{0, \dots, j\}$ is the number of failed B_ψ 's, $s = \pm$ is the sign chosen by the successful $(r+1)$ th B_ψ (if $r < j$) or randomly (if $r = j$), and \mathbf{U} is an $(m-r)$ -element tuple composed of “ ϕ ,” “ ψ ,” and “ f ” (failure) indicating the outcomes of the BSM_{phy} 's from the $(r+1)$ th to the the last. (If $r < j$, the first component of \mathbf{U} is always ψ and the other components are determined by the B_s 's. If $r = j$, all the components are determined by the B_s 's.) Let $N_e(\mathbf{U})$ for $e \in \{\phi, \psi, f\}$ denote the number of e in \mathbf{U} . Then a BSM_{blc} outcome O is included in one of the following $j+3$ events:

$$\begin{aligned} \mathcal{S}_r &:= \{(r, s, \mathbf{U}) | N_f(\mathbf{U}) = 0\} \quad (0 \leq r \leq j), \\ \mathcal{F} &:= \{(j, s, \mathbf{U}) | N_f(\mathbf{U}) = m - j\}, \\ \mathcal{D} &:= \mathcal{O} \setminus \left[\mathcal{F} \cup \bigcup_{r=0}^j \mathcal{S}_r \right], \end{aligned} \quad (5)$$

where \mathcal{O} is the set of all possible outcomes. The probability that each event occurs and the error probabilities ($q_{\text{sign}}^{\text{blc}}, q_{\text{lett}}^{\text{blc}}$) conditioning to the event are explicitly presented in Table I. Note that, if $\eta = 0$, the events \mathcal{S}_r , \mathcal{F} , and \mathcal{D} correspond to success, failure, and sign discrimination. We show these results one by one from now on.

TABLE I. The error probabilities and the total probabilities of the $j+3$ events defined in Eq. (5) for the outcome of a BSM_{blc} in a CBSM using on-off detectors. We define $x := (1 - \eta)^2$, where η is the photon loss rate.

Event (\mathcal{E})	Sign error probability ($q_{\text{sign}}^{\text{blc}}$)	Letter error probability ($q_{\text{lett}}^{\text{blc}}$)	Total probability ($p_{\mathcal{E}}$)
\mathcal{S}_r ($0 \leq r \leq j$)	0	$1/2 - [x/(2-x)]^r/2$	$(1 - x/2)^r x^{m-r}/2$
\mathcal{F}	$(1 - x)^{m-j} / [1 + (1 - x)^{m-j}]$	$1/2$	$(1 - x/2)^j [1 + (1 - x)^{m-j}] / 2$
\mathcal{D}	0	$1/2$	$1 - \sum_r p_{\mathcal{S}_r} - p_{\mathcal{F}}$

Before that, we note that every positive operator-valued measure (POVM) element of a lossy BSM_{phy} has vanishing off-diagonal entries in the Bell basis; see Sec. IV for the proof. Also, each POVM element of a lossy BSM_{blc} , denoted

by M_O^{blc} for each outcome $O = (r, s, \mathbf{U})$, is the tensor product of particular POVM elements of the lossy BSM_{phy}'s constituting the BSM_{blc}. Thus, the conditional probability of getting O from a block-level Bell state $|B\rangle$ is

$$\mathbf{Pr}(O|B) = \langle B| M_O^{\text{blc}} |B\rangle = \frac{1}{2^{m-1}} \sum_i \langle B_i| M_O^{\text{blc}} |B_i\rangle = \frac{1}{2^{m-1}} \sum_i \mathbf{Pr}(O|B_i),$$

where $|B_i\rangle$'s are the terms constituting the summation in Eqs. (1c) or (1d), namely, $|B\rangle = \frac{1}{\sqrt{2^{m-1}}} \sum_i |B_i\rangle$. In other words, when calculating $\mathbf{Pr}(O|B)$, it is enough to find $\mathbf{Pr}(O|B_i)$'s and then take their average.

The posterior probability of a block-level Bell state $|B\rangle$ under a given outcome O is

$$\mathbf{Pr}(B|O) = \frac{\mathbf{Pr}(O|B)}{\sum_{|B'\rangle \in \mathcal{B}_{\text{blc}}} \mathbf{Pr}(O|B')}, \quad (6)$$

where \mathcal{B}_{blc} is the set of the four block-level Bell states. Thus, the result of the BSM_{blc} is selected randomly in the set $R(O) := \text{argmax}_B \mathbf{Pr}(O|B)$. The sign (letter) error probability as a function of O is

$$q_{\text{sign}(\text{lett})}^{\text{blc}}(O) = \frac{1}{|R(O)|} \sum_{|B\rangle \in R(O)} [\mathbf{Pr}(F_{\text{sign}(\text{lett})}(B)|O) + \mathbf{Pr}(F_{\text{sign}} \circ F_{\text{lett}}(B)|O)], \quad (7)$$

where $|F_{\text{sign}(\text{lett})}(B)\rangle$ is the Bell state obtained by flipping the sign (letter) from $|B\rangle$ (e.g., $F_{\text{sign}}(\phi^\pm) = \phi^\mp$).

We now calculate the probabilities in Table I one by one. Let us first consider an outcome $O = (r, s, \mathbf{U}) \in \mathcal{S}_r$, where $N_f(\mathbf{U}) = 0$. Regarding a single term in the decomposition of $|\phi_{(m)}^\pm\rangle$ [see Eq. (1c)], if there are total k of $|\psi^\pm\rangle$'s, the first r physical levels contain $k - N_\psi(\mathbf{U})$ of $|\psi^\pm\rangle$'s, which should suffer photon losses by the definition of r . If $r < j$, s selected by the successful $(r+1)$ th B_ψ is certainly \pm , the sign of $|\phi_{(m)}^\pm\rangle$. If $r = j$, the randomly selected s may or may not be corrected; however, the latter case is out of \mathcal{S}_r since all the following B_\mp 's must fail. The remaining $m - r$ BSM_{phy}'s should not suffer photon losses since $N_f(\mathbf{U}) = 0$. Hence, for all \mathbf{U} satisfying $N_f(\mathbf{U}) = 0$, we get

$$\begin{aligned} \mathbf{Pr}\left(r, \pm, \mathbf{U} \middle| \phi_{(m)}^\pm\right) &= \frac{1}{2^{m-1}} \sum_{k: \text{even} \leq r + N_\psi} \binom{r}{k - N_\psi} (1-x)^{k-N_\psi} \frac{1}{2^{\delta_{rj}}} x^{m-r} \\ &= \frac{1}{2^{\delta_{rj}}} \left[\left(1 - \frac{x}{2}\right)^r \left(\frac{x}{2}\right)^{m-r} + (-1)^{N_\psi} \left(\frac{x}{2}\right)^m \right], \\ \mathbf{Pr}\left(r, \mp, \mathbf{U} \middle| \phi_{(m)}^\pm\right) &= 0, \end{aligned} \quad (8)$$

where $N_\psi = N_\psi(\mathbf{U})$. Similarly, we get

$$\begin{aligned} \mathbf{Pr}\left(r, \pm, \mathbf{U} \middle| \psi_{(m)}^\pm\right) &= \frac{1}{2^{\delta_{rj}}} \left[\left(1 - \frac{x}{2}\right)^r \left(\frac{x}{2}\right)^{m-r} - (-1)^{N_\psi} \left(\frac{x}{2}\right)^m \right], \\ \mathbf{Pr}\left(r, \mp, \mathbf{U} \middle| \psi_{(m)}^\pm\right) &= 0. \end{aligned} \quad (9)$$

From Eqs. (6)–(9), we obtain

$$\begin{aligned} q_{\text{sign}}^{\text{blc}}(O) &= 0 =: q_{\text{sign}}^{\text{blc}}(\mathcal{S}_r), \\ q_{\text{lett}}^{\text{blc}}(O) &= \frac{\left(1 - \frac{x}{2}\right)^r \left(\frac{x}{2}\right)^{m-r} - \left(\frac{x}{2}\right)^m}{2 \left(1 - \frac{x}{2}\right)^r \left(\frac{x}{2}\right)^{m-r}} = \frac{1}{2} \left[1 - \left(\frac{x}{2-x}\right)^r \right] =: q_{\text{lett}}^{\text{blc}}(\mathcal{S}_r). \end{aligned} \quad (10)$$

Note that the error probabilities are the same for all $O \in \mathcal{S}_r$. The total probability that the event \mathcal{S}_r occurs is

$$p_{\mathcal{S}_r} := \frac{1}{4} \sum_{O \in \mathcal{S}_r} \sum_{|B\rangle \in \mathcal{B}_{\text{blc}}} \mathbf{Pr}(O|B) = \frac{1}{2} \frac{1}{2^{\delta_{rj}}} \left(1 - \frac{x}{2}\right)^r \left(\frac{x}{2}\right)^{m-r} 2^{m-r-1+\delta_{rj}} = \frac{1}{2} \left(1 - \frac{x}{2}\right)^r x^{m-r},$$

where the factor $2^{m-r-1+\delta_{rj}}$ is the number of possible \mathbf{U} 's for a given value of r .

Next, we consider $O = (j, s, \mathbf{U}) \in \mathcal{F}$, where $N_f(\mathbf{U}) = m - j$, namely, all the B_s 's fail. Regarding a single term in the decomposition of $|\phi_{(m)}^\pm\rangle$, all the $|\psi^\pm\rangle$'s in the first j physical levels should suffer photon losses. If $s = \pm$, all the

following B_{\pm} 's should suffer photon losses as well. If $s = \mp$, all the following B_{\mp} 's fail regardless of photon losses. We thus get

$$\Pr(j, \pm, \mathbf{U} = (f, \dots, f) \mid \phi_{(m)}^{\pm}) = \frac{1}{2^{m-1}} \sum_{\substack{0 \leq k_1 \leq j \\ 0 \leq k_2 \leq m-j \\ k_1+k_2: \text{ even}}} \binom{j}{k_1} \binom{m-j}{k_2} (1-x)^{k_1+m-j} \cdot \frac{1}{2} = \frac{1}{2} \left(1 - \frac{x}{2}\right)^j (1-x)^{m-j},$$

$$\Pr(j, \mp, \mathbf{U} = (f, \dots, f) \mid \phi_{(m)}^{\pm}) = \frac{1}{2} \left(1 - \frac{x}{2}\right)^j,$$

where k_1 (k_2) in the summation indicates the number of $|\psi^{\pm}\rangle$'s in the first j (last $m-j$) physical levels. Similarly, the same results are obtained for $|\psi_{(m)}^{\pm}\rangle$:

$$\Pr(j, \pm, \mathbf{U} = (f, \dots, f) \mid \psi_{(m)}^{\pm}) = \frac{1}{2} \left(1 - \frac{x}{2}\right)^j (1-x)^{m-j},$$

$$\Pr(j, \mp, \mathbf{U} = (f, \dots, f) \mid \psi_{(m)}^{\pm}) = \frac{1}{2} \left(1 - \frac{x}{2}\right)^j.$$

The corresponding error probabilities are

$$q_{\text{sign}}^{\text{blc}}(O) = \frac{(1-x)^{m-j}}{1 + (1-x)^{m-j}} =: q_{\text{sign}}^{\text{blc}}(\mathcal{F}), \quad q_{\text{lett}}^{\text{blc}}(O) = \frac{1}{2} =: q_{\text{lett}}^{\text{blc}}(\mathcal{F})$$

and the total probability of the event \mathcal{F} is

$$p_{\mathcal{F}} = \frac{1}{4} \sum_{s=\pm} \sum_{|B\rangle \in \mathcal{B}_{\text{blc}}} \Pr(j, s, \mathbf{U} = (f, \dots, f) \mid B) = \frac{1}{2} \left(1 - \frac{x}{2}\right)^j [1 + (1-x)^{m-j}].$$

Lastly, we consider $O = (r, s, \mathbf{U}) \in \mathcal{D}$. If $r < j$, $N_f(\mathbf{U}) > 0$ by the definition of \mathcal{D} and $N_f(\mathbf{U}) < m-r$ since the first component of \mathbf{U} is always ψ . If $r = j$, $0 < N_f(\mathbf{U}) < m-j$ by the definition of \mathcal{D} . Therefore, regardless of r , \mathbf{U} contains at least one failure and one success (ψ or ϕ). Thanks to the successful BSM_{phy} 's, the sign of the result is identified without an error. On the other hand, the letter is not identified because of the failures. We can see intuitively without calculation that the letter error probability is 1/2: Even if there is only one failure in \mathbf{U} , the letter information of the corresponding physical-level Bell state is completely lost, considering that the marginal state of a block-level Bell state on a single physical level is $|\phi^{\pm}\rangle\langle\phi^{\pm}| + |\psi^{\pm}\rangle\langle\psi^{\pm}|$. Thus, the block-level letter information (determined by the parity of the number of BSM_{phy} outcomes with ψ) is completely lost as well. To rewrite the results, we get

$$q_{\text{sign}}^{\text{blc}}(\mathcal{D}) = 0, \quad q_{\text{lett}}^{\text{blc}}(\mathcal{D}) = \frac{1}{2}, \quad p_{\mathcal{D}} = 1 - \sum_{r=0}^j p_{\mathcal{S}_r} - p_{\mathcal{F}}.$$

2. Lattice-level BSM (BSM_{lat})

Each n -tuple of events composed of \mathcal{S}_r ($0 \leq r \leq j$), \mathcal{F} , and \mathcal{D} corresponds to a set of possible outcomes of a BSM_{lat} , whose probability can be directly obtained from Table I. Let us consider such an n -tuple $\mathbf{E} = (\mathcal{E}_1, \dots, \mathcal{E}_n)$. A lattice-level sign error occurs when there is an odd number of block-level sign errors and \mathcal{F} is the only event where a block-level sign error may occur; thus, the sign error probability is

$$q_{\text{sign}} = \sum_{i: \text{odd} \leq N_{\mathcal{F}}} \binom{N_{\mathcal{F}}}{i} q_{\text{sign}}^{\text{blc}}(\mathcal{F})^i [1 - q_{\text{sign}}^{\text{blc}}(\mathcal{F})]^{N_{\mathcal{F}}-i} = \frac{1}{2} - \frac{1}{2} [1 - 2q_{\text{sign}}^{\text{blc}}(\mathcal{F})]^{N_{\mathcal{F}}},$$

where $N_{\mathcal{F}}$ is the number of \mathcal{F} 's in \mathbf{E} .

A lattice-level letter error occurs when the weighted majority vote of the block-level letters gives a wrong answer. We consider i.i.d. random variables $\Lambda_1, \dots, \Lambda_n$ such that $\Lambda_i \sim \text{Bernoulli}(q_i)$ for each i where $q_i := q_{\text{lett}}^{\text{blc}}(\mathcal{E}_i)$, which indicates whether a letter error occurs in the i th block. A lattice-level letter error occurs if

$$\sum_i (2\Lambda_i - 1) \log \frac{1 - q_i}{q_i} =: V(\Lambda_1, \dots, \Lambda_n)$$

is larger than zero or if it is equal to zero and the randomly selected letter is wrong. Therefore, we get

$$\begin{aligned}
q_{\text{lett}} &= \mathbf{Pr}(V(\Lambda_1, \dots, \Lambda_n) > 0) + \frac{1}{2} \mathbf{Pr}(V(\Lambda_1, \dots, \Lambda_n) = 0) \\
&= \sum_{(\lambda_1, \dots, \lambda_n) \in \mathbb{Z}_2^n} \prod_{i=1}^n \mathbf{Pr}(\Lambda_i = \lambda_i) \left\{ \Theta[V(\lambda_1, \dots, \lambda_n) > 0] + \frac{1}{2} \Theta[V(\lambda_1, \dots, \lambda_n) = 0] \right\} \\
&= \sum_{(\lambda_1, \dots, \lambda_n) \in \mathbb{Z}_2^n} \prod_{i=1}^n \left[q_i^{\lambda_i} (1 - q_i)^{1 - \lambda_i} \right] \left[\frac{1}{2} \text{sgn}(V(\lambda_1, \dots, \lambda_n)) + \frac{1}{2} \right], \\
&= \frac{1}{2} + \frac{1}{2} \sum_{(\lambda_1, \dots, \lambda_n) \in \mathbb{Z}_2^n} \prod_{i=1}^n \left[q_i^{\lambda_i} (1 - q_i)^{1 - \lambda_i} \right] \text{sgn} \left(\sum_{i=1}^n (2\lambda_i - 1) \log \frac{1 - q_i}{q_i} \right),
\end{aligned}$$

where $\Theta[C]$ for a condition C is equal to 1 if C is true and 0 if it is false, and $\text{sgn}(a)$ is $a/|a|$ if $a \neq 0$ and 0 if $a = 0$.

IV. PROOF OF VANISHING OFF-DIAGONAL ENTRIES OF THE POVM ELEMENTS OF A LOSSY BSM_{phy}

Here, we prove that every POVM element of a lossy BSM_{phy} in a CBSM with on-off detectors has vanishing off-diagonal entries in the Bell basis. Let Λ_η denote the photon loss channel of a loss rate η defined as $\Lambda_\eta(\sigma) := (1 - \eta)\sigma + \eta|0\rangle\langle 0|$ for a single-photon state σ and the vacuum state $|0\rangle$. By substituting $\sigma = |\psi\rangle\langle\psi|$ for an arbitrary pure state $|\psi\rangle = \alpha|H\rangle + \beta|V\rangle$, we get $\Lambda_\eta(|H\rangle\langle V|) = (1 - \eta)|H\rangle\langle V|$. Thus,

$$\begin{aligned}
(\Lambda_\eta \otimes \Lambda_\eta)(|\phi^\pm\rangle\langle\psi^\pm|) &= (1 - \eta)^2 |\phi^\pm\rangle\langle\psi^\pm| + \eta(1 - \eta)(|H0\rangle\langle V0| + |V0\rangle\langle H0| + |0H\rangle\langle 0V| + |0V\rangle\langle 0H|), \\
(\Lambda_\eta \otimes \Lambda_\eta)(|\phi^\pm\rangle\langle\psi^\mp|) &= (1 - \eta)^2 |\phi^\pm\rangle\langle\psi^\mp| + \eta(1 - \eta)(|H0\rangle\langle V0| - |V0\rangle\langle H0| - |0H\rangle\langle 0V| + |0V\rangle\langle 0H|), \\
(\Lambda_\eta \otimes \Lambda_\eta)(|\phi^+\rangle\langle\phi^-|) &= (1 - \eta)^2 |\phi^+\rangle\langle\phi^-| + \eta(1 - \eta)(|H0\rangle\langle H0| - |V0\rangle\langle V0| + |0H\rangle\langle 0H| - |0V\rangle\langle 0V|), \\
(\Lambda_\eta \otimes \Lambda_\eta)(|\psi^+\rangle\langle\psi^-|) &= (1 - \eta)^2 |\psi^+\rangle\langle\psi^-| + \eta(1 - \eta)(|H0\rangle\langle H0| - |V0\rangle\langle V0| - |0H\rangle\langle 0H| + |0V\rangle\langle 0V|).
\end{aligned} \tag{11}$$

Now, let M_\pm and M_f denote the POVM elements of a lossy B_ψ corresponding to the outcomes $|\psi^\pm\rangle$ and failure, respectively. By modelling a lossy B_ψ as a photon loss channel followed by an ideal B_ψ , M_i for $i \in \{+, -, f\}$ satisfies

$$\text{Tr}[M_i \rho] = \text{Tr}[\Pi_i(\Lambda_\eta \otimes \Lambda_\eta)(\rho)], \tag{12}$$

for any two-qubit state ρ , where

$$\begin{aligned}
\Pi_+ &:= |\psi^+\rangle\langle\psi^+|, \quad \Pi_- := |\psi^-\rangle\langle\psi^-|, \\
\Pi_f &:= |\phi_+\rangle\langle\phi_+| + |\phi_-\rangle\langle\phi_-| + |H0\rangle\langle H0| + |V0\rangle\langle V0| + |0H\rangle\langle 0H| + |0V\rangle\langle 0V| + |00\rangle\langle 00|
\end{aligned}$$

are the projectors of an ideal B_ψ with a lossy input. From Eqs. (11) and (12), we obtain $\langle\psi^\pm| M_i |\phi^\pm\rangle = \langle\psi^\pm| M_i |\phi^\mp\rangle = \langle\phi^\pm| M_i |\phi^-\rangle = \langle\psi^+| M_i |\psi^-\rangle = 0$ for every $i \in \{+, -, f\}$. Similar arguments can be done for a lossy B_+ and B_- as well.

V. MICROCLUSTERS FOR PTQC

In this section, we first derive the physical-level graph structures of post- H microclusters required for PTQC and then present the method to generate them.

A. Physical-level graph structures of post- H microclusters

The physical-level graph structures of the central and side post- H microclusters are shown in Fig. 2 for the two H -configurations. Here, the squares (circles) indicate lattice-level (physical-level) qubits. If a square (circle) is filled with black, it means that the lattice-level (physical-level) Hadamard gate is applied to the qubit after the edges on the qubits are connected. Recurrent subgraphs are abbreviated as blue dashed squares or circles with numbers; see Fig. 2(b) for the detailed interpretation of the notations.

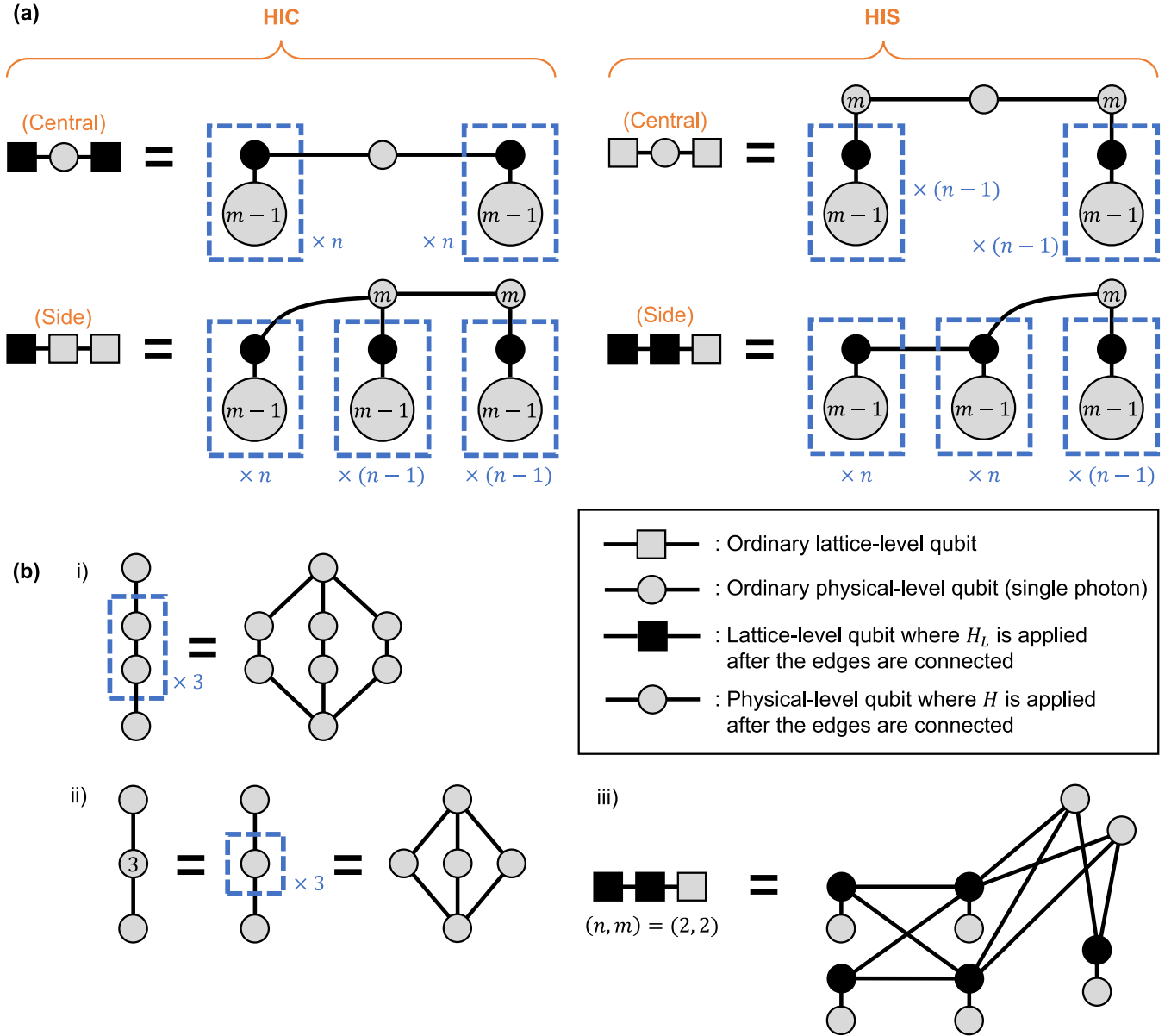


FIG. 2. In (a), the physical-level graph structures of post- H microclusters are shown for the HIC and HIS configurations when the (n, m) parity-state encoding is used. The squares (circles) indicate lattice-level (physical-level) qubits and black squares (circles) mean that the lattice-level (physical-level) H gates are applied to the qubits after the edges on the qubits are connected. A blue dashed box indicates a group of recurrent subgraphs; that is, the structure in the box is repeated as many times as indicated, and if there is an edge across the border of the box, it means that edges of the same shape exist in each of the repeated structures. See i) of (b) for an example. A number inside a circle means a blue dashed box surrounding only the circle with the indicated repetition number, as shown in the example of ii) of (b). If there is an edge between two blue dashed boxes or circles containing numbers, the full graph can be recovered just by expanding them one by one. As an example, the full graph of the side microcluster of the HIS configuration is shown in iii) of (b).

The first step of deriving the graph structures is to investigate how a cluster state is transformed if a Hadamard gate (H_1) is applied on one of the qubits (say, qubit 1) and then a CZ gate (C_{12}^Z) is applied on qubit 1 and another qubit (say, qubit 2) that is not adjacent to qubit 1. Note that, in the Heisenberg picture, the CZ gate transforms the Pauli-X operators of the qubits as $X_1 \rightarrow X_1 Z_2$ and $X_2 \rightarrow Z_1 X_2$, while it leaves the Pauli-Z operators the same. For a qubit i , $S_i := X_i \prod_{j \in N(i)} Z_j$, where $N(i)$ is the set of qubits adjacent to qubit i , is a stabilizer of the initial cluster

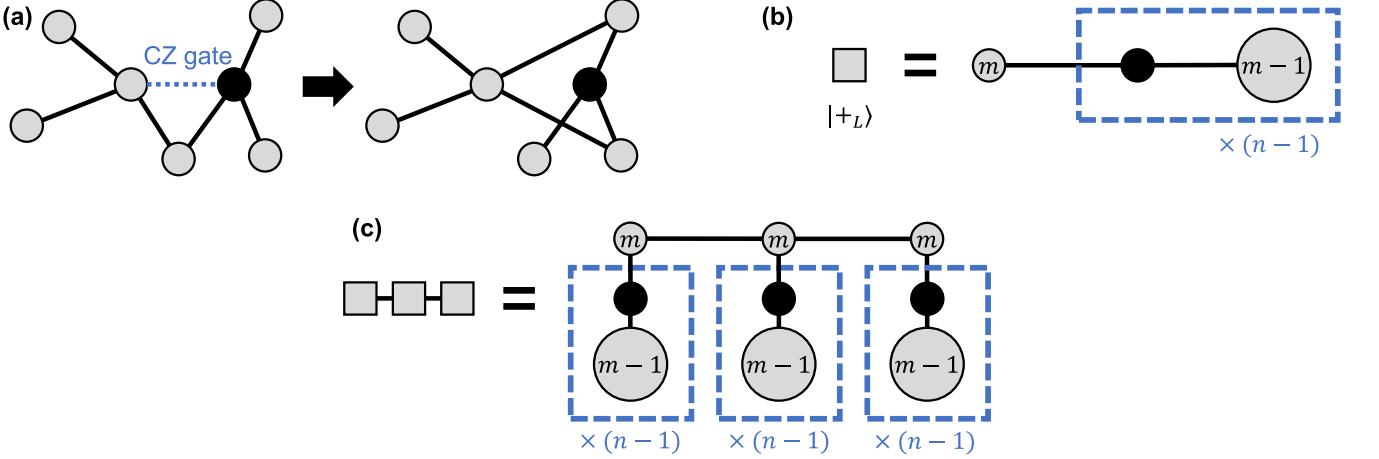


FIG. 3. (a) Transformation of a cluster state by applying a Hadamard gate followed by applying a CZ gate. (b) Physical-level graph structure of the state $|+L\rangle = |0_L\rangle + |1_L\rangle$. (c) Physical-level graph structure of a lattice-level three-qubit linear cluster state.

state. The stabilizers S_1 and S_1S_2 are transformed by $C_{12}^Z H_1$ as

$$S_1 = X_1 \prod_{j \in N(1)} Z_j \longrightarrow Z_1 \prod_{j \in N(1)} Z_j = H_1 \left(X_1 \prod_{j \in N(1)} Z_j \right) H_1,$$

$$S_1S_2 = X_1X_2 \prod_{j \in N(1) \Delta N(2)} Z_j \longrightarrow X_2 \prod_{j \in N(1) \Delta N(2)} Z_j = H_1 \left(X_2 \prod_{j \in N(1) \Delta N(2)} Z_j \right) H_1,$$

where $A \Delta B := A \cup B \setminus (A \cap B)$ for two sets A and B . Also, for each qubit $i \in N(1)$,

$$S_i = X_i \prod_{j \in N(i)} Z_j \longrightarrow X_i X_1 Z_2 \prod_{j \in N(i) \setminus \{1\}} Z_j = H_1 \left(X_i \prod_{j \in N(i) \Delta \{2\}} Z_j \right) H_1.$$

Therefore, the overall effect of the process is, for each qubit i adjacent to qubit 1, to flip the connectivity of the qubits 2 and i (namely, connect them if they are disconnected and disconnect them if they are already connected) and then apply H_1 . An example of this transformation is presented in Fig. 3(a).

Next, we obtain the graph structure of the state $|+L\rangle := |0_L\rangle + |1_L\rangle$. Figure 4 shows the encoding circuit of the state for the $(3, 3)$ parity-state encoding, which employs multiple copies of the state $|+\rangle := |H\rangle + |V\rangle$, CZ gates, and Hadamard gates. Here, we label the j th physical qubit of the i th block by $[i, j]$. It is straightforward to generalize it for any pair of (n, m) . The graph structure of $|+L\rangle$ shown in Fig. 3(b) is obtained by preparing nm isolated vertices and tracking the transformation of the graph via the CZ and Hadamard gates in the circuit.

A lattice-level CZ gate C_L^Z is done by m^2 physical CZ gates:

$$C_L^Z = \prod_{i,j \leq m} C_{1i,1j}^Z, \quad (13)$$

where $C_{ij,kl}^Z$ is the CZ gate between the $[i, j]$ qubit of the first lattice-level qubit and the $[k, l]$ qubit of the second lattice-level qubit. It can be verified as follows: The stabilizer generators of the (n, m) parity-state encoding are

$$\left\{ X_{ij} X_{i(j+1)} \quad (\forall i \leq n, \forall j \leq m-1), \quad \prod_{j=1}^m Z_{ij} Z_{(i+1)j} \quad (\forall i \leq n-1) \right\}$$

and the lattice-level Pauli operators are

$$X_L = X_{11} \cdots X_{n1}, \quad Z_L = Z_{11} \cdots Z_{1m},$$

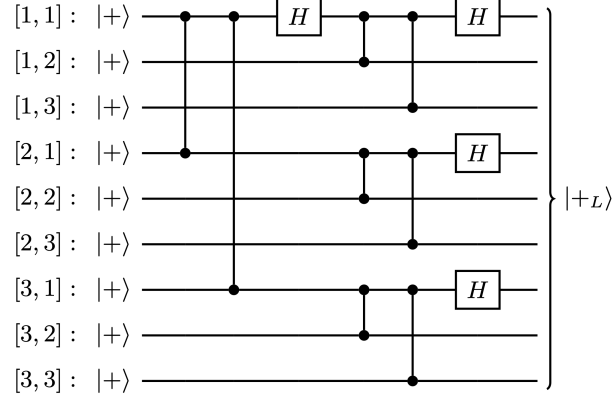


FIG. 4. Encoding circuit of the state $|+_L\rangle := |0_L\rangle + |1_L\rangle$ in the $(3, 3)$ parity-state encoding, which employs multiple copies of the state $|+\rangle := |h\rangle + |v\rangle$, cz gates, and Hadamard gates. The label $[i, j]$ for each physical-level qubit indicates the index i of the block and the index j of the photon in the block.

where X_{ij} (Z_{ij}) is the Pauli- X ($-Z$) operator on the $[i, j]$ qubit. It is straightforward to see that the RHS of Eq. (13) commutes with all the stabilizers and transforms the lattice-level Pauli operators correctly.

Combining the above results on the $|+_L\rangle$ state and the lattice-level cz gate, we attain the graph structure of a lattice-level three-qubit linear cluster state shown in Fig. 3(c). The only left ingredient is the lattice-level Hadamard gate (H_L). The circuit for H_L is obtained by simply connecting the decoding circuit, the physical Hadamard gate, and the encoding circuit, which is explicitly shown in Fig. 5 for the $(3, 3)$ parity-state encoding. By transforming the graph in Fig. 3(c) with appropriate lattice-level Hadamard gates, we finally get the desired graph structures of the post- H microclusters shown in Fig. 2. Note that, for central microclusters, the middle lattice-level qubits are replaced with unencoded physical-level qubits.

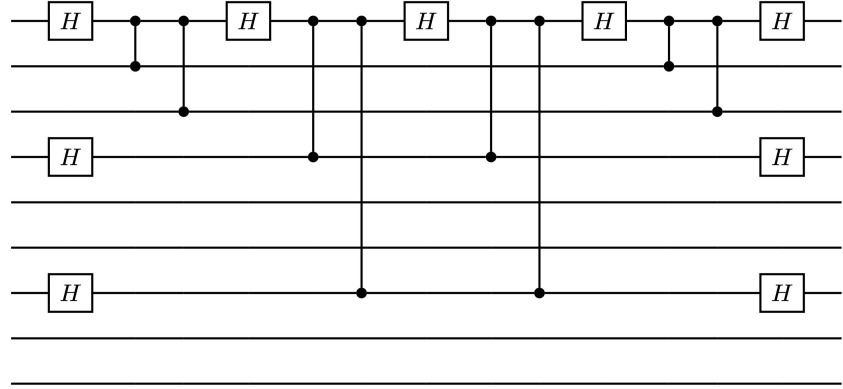


FIG. 5. Circuit to implement the lattice-level Hadamard gate of the $(3, 3)$ parity-state encoding.

B. Generation of post- H microclusters

We now describe the generation of post- H microclusters. The physical-level graphs of post- H microclusters (see Fig. 2) can be decomposed into fusions of multiple components through the process shown in Fig. 6: Each recurrent subgraph connected with multiple vertices is separated and connected with only one vertex. The results are shown in Fig. 7. Therefore, the post- H microclusters can be generated by preparing individual components first and then merging them through fusions. For microclusters that are not shown in the figure (including the central microcluster of HIC and the other microclusters that do not meet the presented conditions), the decomposition is not necessary; that is, the entire physical-level graph itself is a single component. This process may greatly reduce the number of required fusions since the number of edges decreases as shown in Fig. 6.

Each component of the decomposition of a post- H microcluster can be generated by performing fusions on multiple

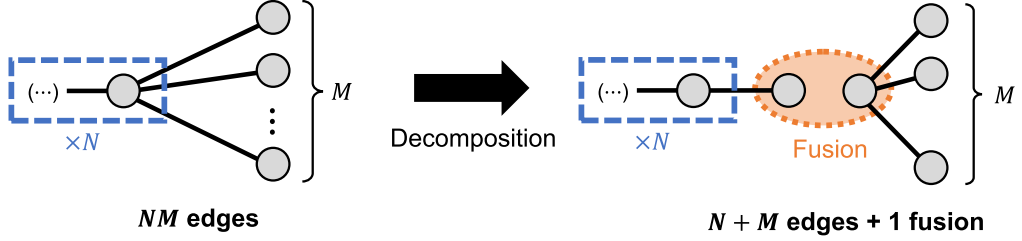


FIG. 6. Decomposition of a cluster state by separating recurrent subgraphs that are connected with multiple vertices.

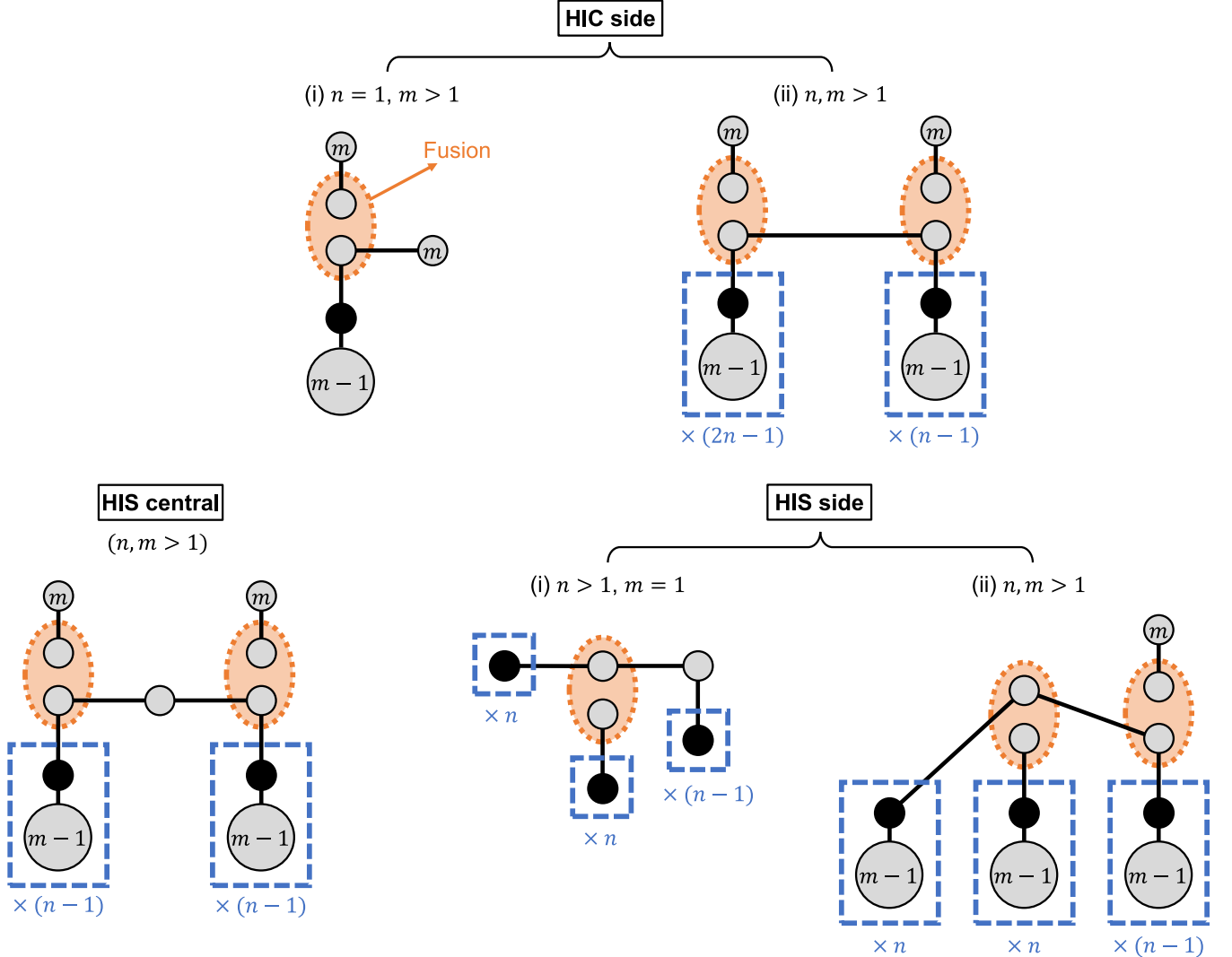


FIG. 7. Decomposition of post- H microclusters into multiple components done by separating connected pairs of recurrent subgraphs. Individual components are prepared first and then merged through fusions to construct post- H microclusters. The post- H microclusters that are not presented here do not have connected pairs of recurrent subgraphs.

GHZ-3 states. Let us define the *GHZ- l state* for an integer $l \geq 3$ by the state $|\text{GHZ}_l\rangle := |\text{H}\rangle^{\otimes l} + |\text{V}\rangle^{\otimes l}$. Note that it is a state obtained from a cluster state with a star graph (where the number of vertices is l) by applying Hadamard gates on all the leaves of the graph; namely,

$$|\text{GHZ}_l\rangle = H_2 \cdots H_l C_{12}^Z \cdots C_{1l}^Z |+\rangle^{\otimes l}.$$

We refer to the first photon of the above expression as the *root photon* of the state and the other photons as its

leaf photons. The root photon can be chosen arbitrarily since the state is symmetric about the permutations of the photons.

If a BSM is performed on the root photon of a GHZ- l_1 state and a leaf photon of a GHZ- l_2 state, the resulting state on the remaining photons is a GHZ- $(l_1 + l_2 - 2)$ state; see Fig. 8(a) for an example. Thus, an arbitrary GHZ state can be constructed by performing BSMs on multiple GHZ-3 states appropriately. On the other hand, if a fusion is performed on two leaf photons respectively selected from these two GHZ states, the resulting state is no longer a GHZ state, but it is a cluster state (up to some Hadamard gates) with a graph containing a vertex with degree $l_1 - 1$, a vertex with degree $l_2 - 1$, and multiple vertices with degree one; see Fig. 8(b) for an example. (The degree d_v of a vertex v means the number of edges connected to v .) Combining the above facts, an arbitrary cluster state $|G\rangle$ can be generated from GHZ-3 states in the following way: For each vertex v of G with a degree larger than one, prepare a GHZ- $(d_v + 1)$ state through BSMs on GHZ-3 states. Then, for each edge of G , perform a fusion across the two GHZ states corresponding to the vertices connected by the edge. Lastly, apply a Hadamard gate for every remaining leaf photon. We refer to each BSM or fusion during the process as a *merging operation*.

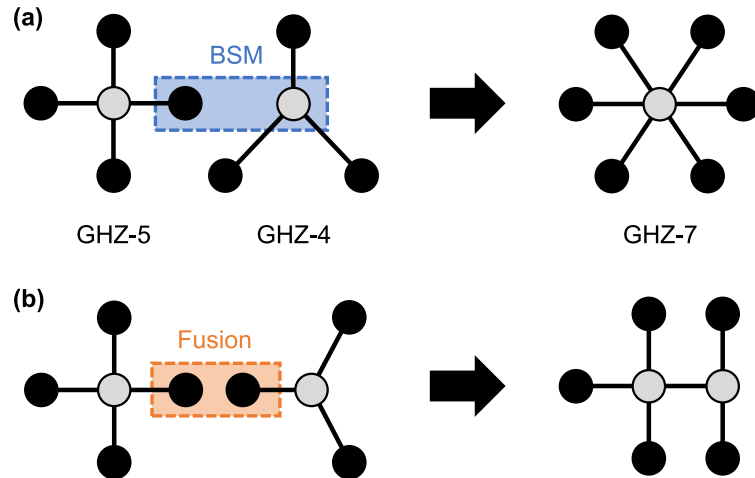


FIG. 8. Examples of the two types of merging operations on two GHZ states: (a) a BSM on the root photon of one state and a leaf photon of the other and (b) a fusion on two leaf photons.

Following the aforementioned method, any component of post- H microclusters can be generated up to several physical-level Hadamard gates. However, the method can be generalized further by using the fact that all the merging operations during the process commute; in other words, we can freely choose their order. It is not even necessary to prepare GHZ states first and then merge them through fusions. We define a *merging graph* of a cluster state by a graph where the vertices correspond to initial GHZ-3 states and the edges indicate the merging operations on them. Each edge of a merging graph is either *internal* or *external*: Internal (external) edges correspond to BSMs (fusions) performed across the two GHZ-3 states at the ends of the edge. Also, some vertices of a merging graph are *seed vertices*, which means that, for each seed vertex, one of the photons of the corresponding GHZ-3 state does not participate in any merging operation and remains in the final cluster state. Note that multiple merging graphs may be possible for one cluster state.

We now present a systematic algorithm to construct a merging graph G_{mrg} of the cluster state $|G\rangle$ for a graph $G = (V_0, E_0)$ (see Fig. 9 for two examples):

1. Initialize the graph $G_{\text{mrg}} = (V, E)$ by G ; that is, $V \leftarrow V_0, E \leftarrow E_0$.
2. Let us define $V_{\text{deg} \geq 3} := \{v \in V | d_v \geq 3\}$. This set is fixed and not updated during the entire process. For each vertex $v \in V_{\text{deg} \geq 3}$, perform the follows:
 - (a) Remove v from G_{mrg} and add $d_v - 1$ new vertices. Let $V_{\text{new}} = (v_{\text{new}}^{(1)}, \dots, v_{\text{new}}^{(d_v-1)})$ denote the series of the new vertices and $V_{\text{ngh}} = (v_{\text{ngh}}^{(1)}, \dots, v_{\text{ngh}}^{(d_v)})$ denote the series of the vertices that were adjacent to v before removing it. The order of the vertices in V_{ngh} can be arbitrarily chosen.
 - (b) Connect the vertices in V_{new} linearly with *internal* edges; namely, connect $(v_{\text{new}}^{(1)}, v_{\text{new}}^{(2)})$, $(v_{\text{new}}^{(2)}, v_{\text{new}}^{(3)})$, and so on.

(c) Choose one of the vertices in V_{new} arbitrarily and term it the seed vertex v_{seed} of v_0 , where v_0 is the vertex in G from which v originates.

(d) Let us define V'_{new} by omitting v_{seed} from V_{new} while keeping the order of the other vertices. For each $i \in \{1, \dots, d_v - 2\}$, connect $v_{\text{ngh}}^{(i)}$ and the i th element of V'_{new} with an *external* edge.

(e) Connect $(v_{\text{new}}^{(1)}, v_{\text{ngh}}^{(d_v-1)})$ and $(v_{\text{new}}^{(d_v-1)}, v_{\text{ngh}}^{(d_v)})$ with *external* edges.

3. Remove all vertices with degree 1 from the graph. For each vertex $v_0 \in V_0$ with degree 2, if v is the vertex in V originating from v_0 (which is not removed in the previous steps), define the seed vertex of v_0 as v .

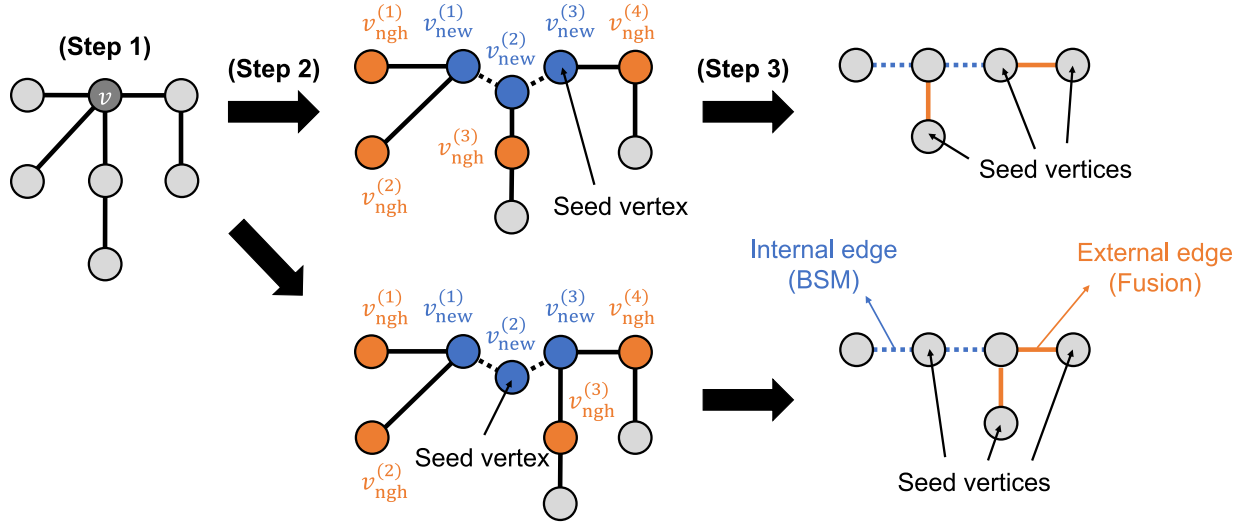


FIG. 9. Construction of merging graphs from the graph of a cluster state. v is the only vertex with a degree larger than two in the original graph. The upper and lower processes differ in the selection of the seed vertex for the decomposition of v .

Each iteration of the second step (for a vertex v) in the above process indicates decomposing the GHZ- $(d_v + 1)$ state into $d_v - 1$ GHZ-3 states, which is done by adding $d_v - 1$ new vertices connected with each other by internal edges. What matters is the way to distribute d_v edges connected with v to the new vertices. Considering that each new vertex can be connected with at most three edges (since it corresponds to a GHZ-3 state), total $d_v + 1$ edges can be connected with the new vertices in addition to the internal edges. However, the number of the external edges is d_v , thus one of the new vertices should be connected with only two edges, which is the seed vertex.

Lastly, we present the most general method to create a post- H microcluster, combining the above results. Since the fusions performed across different components shown in Fig. 7 also commute with every merging operation for the generation of the components, we can combine these two separate processes into one. We construct the merging graph of a post- H microcluster by combining the merging graphs of its components; namely, if a vertex v_0 of a component and a vertex v_1 of another component need to be fused, we connect the seed vertices of v_0 and v_1 with an external edge in the combined merging graph. With the obtained merging graph, we can construct the post- H microcluster up to physical-level Hadamard gates by performing fusions and BSMs on multiple GHZ-3 states according to the edges regardless of their time order.

Note that there are three types of degrees of freedom for the process of generating a post- H microcluster: (i) the order of the series V_{ngh} and (ii) the selection of the seed vertex for each vertex with a degree larger than 2 in each component and (iii) the time order of all the merging operations. These factors may severely affect the resource overhead, as discussed in Sec. VI.

VI. DETAILS OF RESOURCE ANALYSIS ON PTQC

Here, we describe the details of resource analysis on PTQC. We first investigate calculating N_{GHZ}^* , the expected number of required GHZ-3 states to generate one star cluster. N_{GHZ}^* is used to obtain the expected total number $N_{p_L^{\text{targ}}}$ of GHZ-3 states to achieve the target logical error rate of p_L^{targ} for the logical identity gate with the length of

$d - 1$ unit cells. Let $N_{\text{GHZ}}^{\text{central}}$ ($N_{\text{GHZ}}^{\text{side}}$) denote the expected number of required GHZ-3 states to generate one central (side) microcluster. Then we get

$$N_{\text{GHZ}}^* = \begin{cases} [(N_{\text{GHZ}}^{\text{central}} + N_{\text{GHZ}}^{\text{side}})/p_{\text{succ,step1}} + N_{\text{GHZ}}^{\text{side}}]/p_{\text{succ,step1}} & \text{if } \text{pssl is True,} \\ N_{\text{GHZ}}^{\text{central}} + 2N_{\text{GHZ}}^{\text{side}} & \text{if } \text{pssl is False,} \end{cases} \quad (14)$$

where $p_{\text{succ,step1}}$ is the average success probability of step-1 fusions and **pssl** is defined in Sec. VII. Each microcluster is generated by merging multiple GHZ-3 states via BSMs or fusions according to a merging graph, as presented in Sec. V B. We consider using only microclusters generated without failed merging operations.

Note that, if two cluster states composed of physical-level qubits respectively require N_1 and N_2 of GHZ-3 states to generate, it averagely requires

$$N_1 +_f N_2 := \frac{2}{(1 - \eta)^2}(N_1 + N_2), \quad (15)$$

GHZ-3 states to successfully generate their merged cluster state. The factor $2/(1 - \eta)^2$ is the inverse of the success probability of the fusion. Since $+_f$ is not associative, the merging order is important when merging three or more cluster states.

For the generation of a post- H microcluster $|\text{MC}\rangle$, $N_{\text{GHZ}}^{\text{MC}}$ ($N_{\text{GHZ}}^{\text{central}}$ or $N_{\text{GHZ}}^{\text{side}}$) is affected by three types of degrees of freedoms: (i) the order of the series V_{ngb} and (ii) the selection of the seed vertex for each vertex with degree larger than 2 in each component of the decomposition of $|\text{MC}\rangle$ and (iii) the time order of all the merging operations (see Sec. V B). We take an approach that the factors (i) and (ii) are randomly chosen and the order of the merging operations is selected by an algorithm found heuristically. The following process is used to compute $N_{\text{GHZ}}^{\text{MC}}$:

1. Construct the merging graphs of the components of $|\text{MC}\rangle$ by the process in Sec. V B. Here, for each iteration of step 2 of the process, the order of the series V_{ngb} and the seed vertex are randomly selected.
2. Construct the merging graph G_{mrg} of $|\text{MC}\rangle$ by combining the merging graphs of the components, as described in Sec. V B.
3. Allocate a weight of 1 to every vertex in G_{mrg} . Let N_v denote the weight of vertex v . For an edge e connecting v_1 and v_2 , define $N_e := N_{v_1} +_f N_{v_2}$.
4. Repeat the following until G_{mrg} has only one vertex.
 - (a) Find the set $E_{\text{min,wgt}}$ of edges with the smallest value of N_e .
 - (b) Using an edge coloring algorithm, allocate “colors” to all edges so that different edges sharing a vertex have different colors and as few colors as possible are used.
 - (c) Partition $E_{\text{min,wgt}}$ into disjoint subsets by the colors of the edges. Find the largest subset E_{mrg} among them. If such a subset is not unique, choose one randomly.
 - (d) For each edge e in E_{mrg} , perform the follows.
 - i. Contract the two vertices (v_1, v_2) connected by e into a single vertex v_e . Namely, v_1 and v_2 are replaced with v_e and every edge connected to v_1 or v_2 is connected to v_e instead. This process may make multiple edges connect the same pair of vertices, which is allowed. If there are other edges connecting v_1 and v_2 besides e , they are transformed into loops connected to v_e .
 - ii. Allocate N_e to N_{v_e} .
5. $N_{\text{GHZ}}^{\text{MC}}$ is equal to the weight of the only vertex left in G_{mrg} .

In the middle of the above process, each vertex of G_{mrg} represents a connected subgraph of the intermediate cluster state and its weight is equal to the expected number of GHZ-3 states to construct the subgraph state. Thus, each contraction in step 4(d) corresponds to merging two independent cluster states to form a larger cluster state.

Steps 4(a)–(c) show the strategy to determine the order of the merging operations. Although it may be not an optimal strategy, it is based on the following two intuitions: First, it is better to merge cluster states with small weights first, since $(N_1 +_f N_2) +_f N_3 < N_1 +_f (N_2 +_f N_3)$ if $N_1 < N_2 < N_3$. Secondly, it is better to perform merging operations in parallel as much as possible and the edges with the same color (assigned by an edge coloring algorithm) can be merged parallelly. For coloring edges, we use the greedy graph coloring function (`coloring.greedy_color`) in NetworkX package [3] with the strategy `largest_first`. Since the function performs vertex coloring, we input the line graph of G_{mrg} into the function.

To obtain the simulation results in the main text, we sample 1200 values of $N_{\text{GHZ}}^{\text{MC}}$ through the aforementioned process. Let N_1 (N_2) be the minimal values of $N_{\text{GHZ}}^{\text{MC}}$ for the first 600 (total 1200) samples. If $N_1 = N_2$, the value is returned. If otherwise, we sample 1200 values of $N_{\text{GHZ}}^{\text{MC}}$ again and denote the minimal $N_{\text{GHZ}}^{\text{MC}}$ for the total 2400 samples by N_3 . If $N_2 = N_3$, the value is returned. If otherwise, we sample 2400 merging graphs again and so on. By varying the total number of samples in this way, it is possible to increase the odds that we reach close to the real optimal value.

After obtaining N_{GHZ}^* (at $\eta = \eta_0$), we consider the logical identity gate with $T = d - 1$ (see Fig. 10) to calculate $\mathcal{N}_{p_L^{\text{targ}}}^*$. $\mathcal{N}_{p_L^{\text{targ}}}^*$ is determined by the following equality:

$$\mathcal{N}_{p_L^{\text{targ}}}^* = N_{\text{GHZ}}^*(2d_{p_L^{\text{targ}}} + 1)(3d_{p_L^{\text{targ}}}^2 - 3d_{p_L^{\text{targ}}} + 1),$$

where $d_{p_L^{\text{targ}}}$ is the minimal code distance to achieve the target logical error rate of p_L^{targ} for the identity gate when $\eta = \eta_0$. $d_{p_L^{\text{targ}}}$ is obtained by employing the error simulation method in Sec. VII. However, this method simulates the logical identity gate with $T = 4d + 1$, while our current interest is that with $T = d - 1$. From an obtained logical error rate p_L' from the method with $T = 4d + 1$, we estimate the *logical error rate* $p_L^{(1)}$ *per two layers (one unit cell)* from the relation

$$p_L' = \sum_{t \leq T: \text{odd}} \binom{T}{t} \left(p_L^{(1)} \right)^t \left(1 - p_L^{(1)} \right)^{T-t} = \frac{1}{2} \left[1 - \left(1 - 2p_L^{(1)} \right)^T \right],$$

where $T = 4d + 1$. Using a similar relation for $T = d - 1$, we can convert p_L' into the logical error rate p_L of the gate with $T = d - 1$. We then obtain $d_{p_L^{\text{targ}}}$ by calculating the logical error rate $p_L^{(d)}$ at $\eta = \eta_0$ for each code distance $d \leq 11$ and finding the smallest d satisfying $p_L^{(d)} < p_L^{\text{targ}}$. If $p_L^{(11)} \geq p_L^{\text{targ}}$, $d_{p_L^{\text{targ}}}$ is estimated from the linear extrapolation of the points $(9, \log p_L^{(9)})$ and $(11, \log p_L^{(11)})$.

VII. DETAILS OF ERROR SIMULATIONS

In this section, we describe the error simulation method in detail. We first introduce the parameters that determine the details of PTQC:

- **pssl**: If **True**, star clusters generated by successful step-1 fusions are post-selected for step 2. If **False**, all generated star clusters are used regardless of the fusion results.
- **hic**: If **True**, the H -configuration is HIC. If **False**, it is HIS.
- **tprd**: If **True**, two-photon resolving detectors are used. If **False**, on-off detectors are used.
- n, m : The (n, m) parity-state encoding is used to encode side qubits.
- j : The maximal number of B_ψ 's in a BSM_{blc}. (See the CBSM scheme in Sec. II.)

For a fixed parameter setting, we consider an RHG lattice whose boundaries are in the form of a cuboid as visualized in Fig. 10, which implements a logical identity gate. Let us term the three axes of the cuboid as the x -, y -, and t -axis and the corresponding boundaries as the x -, y -, and t -boundaries. The t -axis is also referred to as the *simulated time axis*. The cuboid has the widths of $d - 1$ unit cells along the x - and y -axis, where d is the code distance, and the width of $T = 4d + 1$ unit cells along the t -axis. The value of T is arbitrarily set to be larger enough than d for reducing the effects of errors near the t -boundaries. The x - and t -boundaries are set to be primal, while the y -boundaries are set to be dual. In other words, the x - and t -boundaries adjoin normally on primal unit cells, while the y -boundaries cross the middle of primal unit cells. For error simulations, we count error chains connecting the opposite x -boundaries, thus we assume that the qubits on the t -boundaries do not have errors.

We use a Monte-Carlo method for the simulations. Each trial is proceeded as follows:

1. Sample the outcomes of all fusions in steps 1 and 2 (only step 2 if **pssl** is **True**) by the probabilities presented in Sec. III, which depend on the values of **tprd**, n , m , j , and η .
2. For each fusion outcome, the corresponding error probabilities (q_{sign} , q_{lett}) are obtained and whether the fusion has a sign or letter error is randomly determined by the probabilities. These error probabilities and errors are then propagated to appropriate central qubits determined by the value of **hic**. For each central qubit i , the presence or absence of an error and its probability are assigned to a boolean variable **error** _{i and a floating-point variable $q_{\text{err},i}$, respectively.}

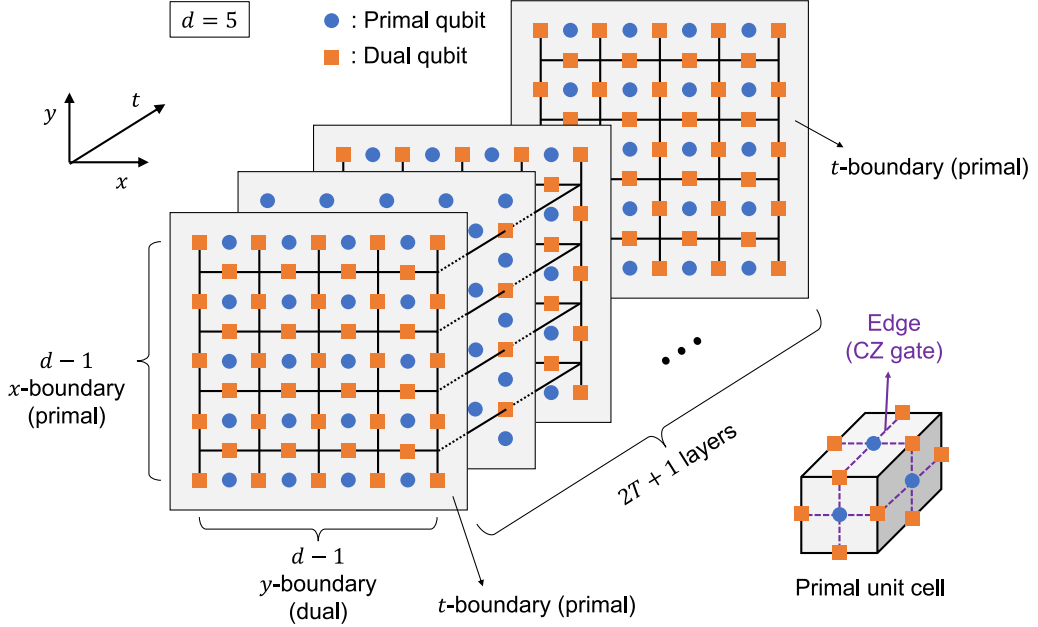


FIG. 10. Structure of a logical identity gate with the code distance of $d = 5$ and the length of T unit cells ($2T + 1$ layers) along the simulated time (t) axis for numerical simulations.

3. For each central qubit i , a photon loss is sampled with probability η . If it has a loss, $q_{\text{err},i}$ is updated to 0.5 and error_i is flipped with probability 50%.
4. The syndrome of each parity-check operator (which corresponds to a primal unit cell) is determined by the values of error_i 's of the qubits in the support of the operator.
5. The syndromes are decoded to infer the locations of the errors. We use the weighted minimum-weight perfect matching decoder via PyMatching package [4] where the weight for each qubit i is $\log[(1 - q_{\text{err},i})/q_{\text{err},i}]$. (If $q_{\text{err},i} = 0$, the weight is infinity, which is handled by ignoring the qubit from the input of the decoder.) Exceptionally, if every value of $q_{\text{err},i}$ is either 0 or 1/2, the qubits with $q_{\text{err},i} = 1/2$ are given the weight of one, not zero, for a technical reason.
6. The remaining errors are obtained by comparing the original and estimated errors. If the number of the remaining errors on one side of the x -boundaries is odd, we regard that this trial has a logical error.

The logical error rate p_L for a given parameter setting is obtained by repeating the above process a sufficient number of times. In detail, we repeat the process until $\Delta p_L/p_L \leq 0.1$ is reached where Δp_L is half the width of the 99% confidence interval. The logical error rates $p_L^{(9)}(\eta)$, $p_L^{(11)}(\eta)$ are calculated while varying η for two code distances $d = 9, 11$ and the loss threshold η_{th} is obtained by finding the largest η satisfying $p_L^{(11)}(\eta) + \Delta p_L^{(11)}(\eta) < p_L^{(9)}(\eta) - \Delta p_L^{(9)}(\eta)$.

VIII. ADDITIONAL SIMULATION RESULTS FOR PTQC

Here, we present additional simulation results on the loss thresholds and resource overheads of PTQC. Figures 11 and 12 respectively show the loss thresholds η_{th} and resource overheads \mathcal{N}_{10-6} for various parameter settings, which are the extended versions of Figs. 4(a) and (b) in the main text. Figure 13 presents the loss thresholds η_{th} as a function of the expected number N_{GHZ}^* of GHZ-3 states required per central qubit at $\eta = \eta_{\text{th}}/2$ for various parameter settings. It shows that the post-selection is also effective in enhancing the resource overheads when two-photon resolving detectors are used, while it is not when on-off detectors are used. The information of the data points along the upper envelopes in Fig. 13 is explicitly listed in Table II.

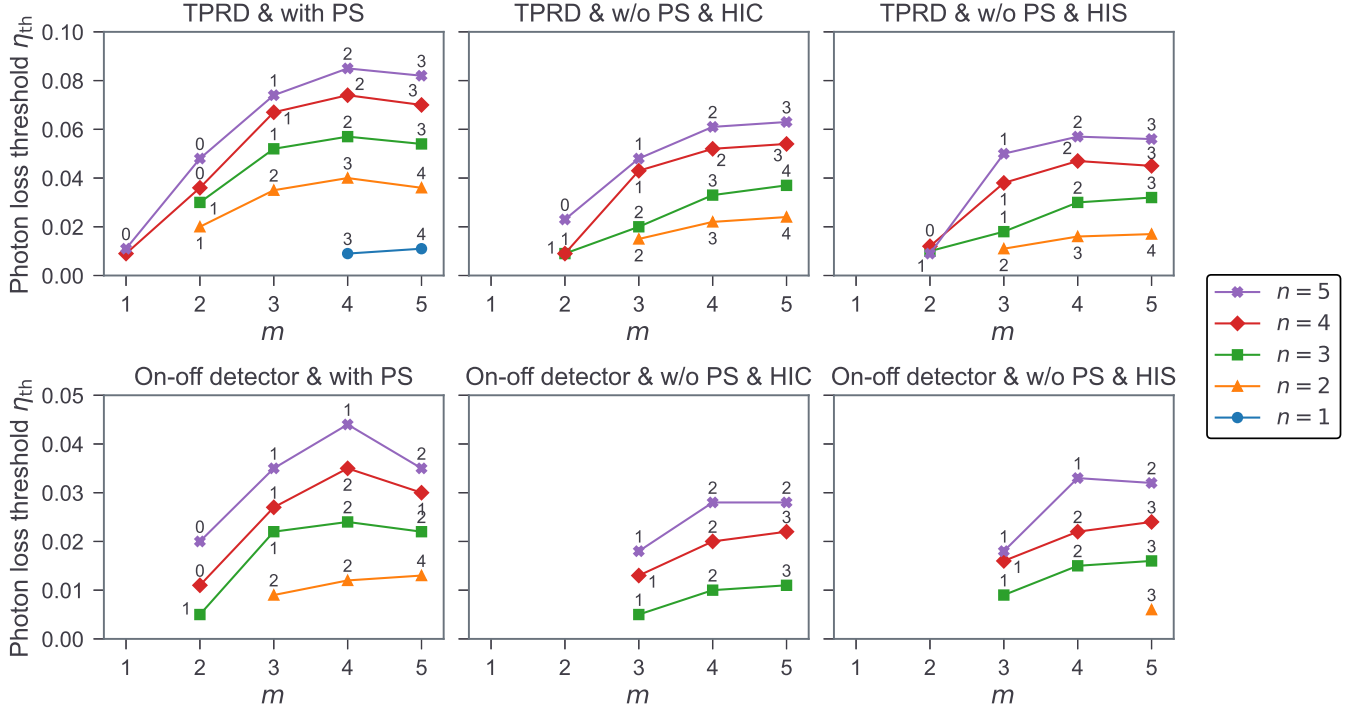


FIG. 11. Loss threshold η_{th} for various parameters on the encoding size (n, m) , the type of detectors, the post-selection (PS) of star clusters, and the H -configuration. “TPRD” stands for a two-photon resolving detector. Only data points with $\eta_{\text{th}} \geq 0.005$ are shown. The values of j are chosen to maximize η_{th} and shown next to the data points. The H -configuration does not affect η_{th} when star clusters are post-selected.

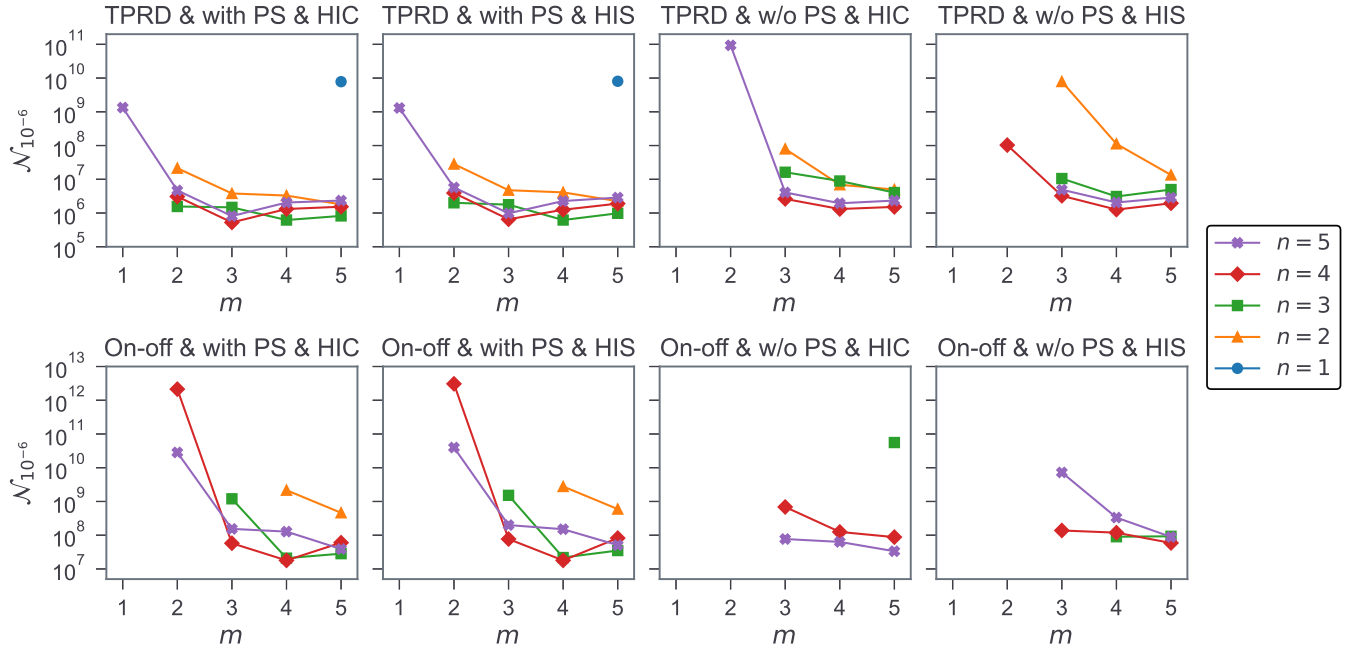


FIG. 12. Resource overhead $\mathcal{N}_{10^{-6}}$ at $\eta = 0.01$ for various parameters on the encoding size (n, m) , the type of detectors, the post-selection (PS) of star clusters, and the H -configuration. $\mathcal{N}_{10^{-6}}$ is defined by the expected total number of GHZ-3 states required to achieve a logical error rate of 10^{-6} . Only data points with $\eta_{\text{th}} > 0.01$ are shown. The values of j used are the same as presented in Fig. 11.

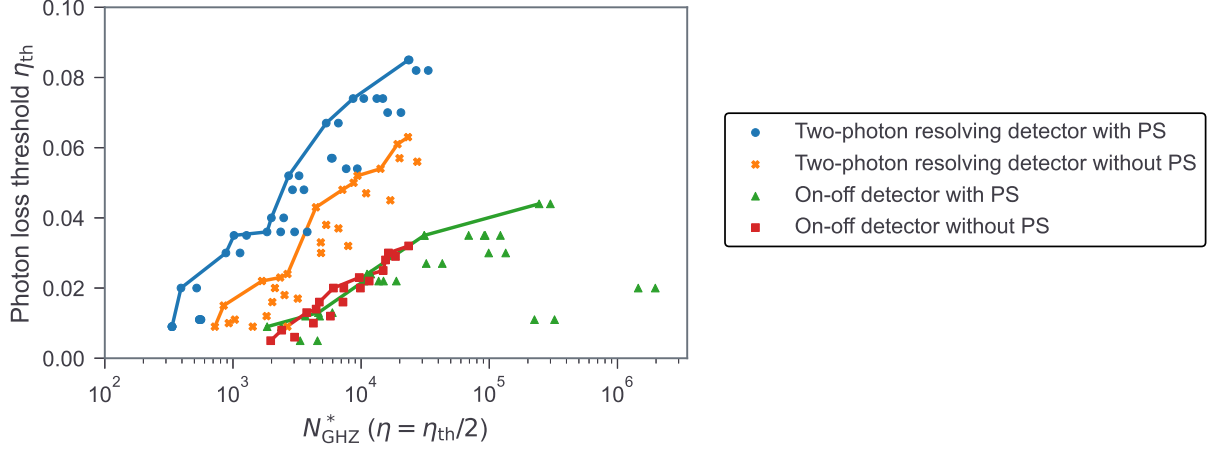


FIG. 13. Photon loss thresholds η_{th} as a function of the number N_{GHZ}^* of GHZ-3 states required per central qubit calculated at $\eta = \eta_{\text{th}}/2$. The data points correspond to different parameter settings on the type of detectors, the post-selection (PS) of star clusters, the encoding size, and the H -configuration, which are grouped by the first two factors. The upper envelope for each of the groups is presented as a line. The information of the data points along the lines is explicitly listed in Table II. The values of j are chosen to maximize η_{th} . Only data points with $\eta_{\text{th}} \geq 0.005$ are shown.

TABLE II. Information of the data points along the upper envelope lines in Fig. 13. N_{GHZ}^* , \mathcal{N}_{10-7} , and d_{10-7} at $\eta = 1\%$ are not calculated when $\eta_{\text{th}} < 1\%$.

η_{th} ($\eta = \eta_{\text{th}}/2$)	N_{GHZ}^* ($\eta = 1\%$)	N_{GHZ}^* ($\eta = 1\%$)	\mathcal{N}_{10-7} ($\eta = 1\%$)	d_{10-7}	n	m	j	H -config.	η_{th} ($\eta = \eta_{\text{th}}/2$)	N_{GHZ}^* ($\eta = \eta_{\text{th}}/2$)	N_{GHZ}^* ($\eta = 1\%$)	\mathcal{N}_{10-7} ($\eta = 1\%$)	d_{10-7}	n	m	j	H -config.		
Two-photon resolving detector with post-selection																			
0.009	3.3×10^2	3.7×10^2			1	4	3	HIC	0.009	7.2×10^2				3	2	1	HIC		
0.02	3.9×10^2	3.9×10^2	2.1×10^7	21	2	2	1	HIC	0.015	8.4×10^2	8.6×10^2	7.9×10^7	25	2	3	2	HIC		
0.03	8.8×10^2	8.2×10^2	1.5×10^6	7	3	2	1	HIC	0.022	1.6×10^3	1.6×10^3	6.8×10^6	9	2	4	3	HIC		
0.035	1.0×10^3	9.2×10^2	3.8×10^6	9	2	3	2	HIC	0.023	2.3×10^3	2.3×10^3	9.3×10^{10}	189	5	2	1	HIC		
0.036	1.8×10^3	1.6×10^3	3.0×10^6	7	4	2	1	HIC	0.024	2.6×10^3	2.6×10^3	4.9×10^6	7	2	5	4	HIC		
0.04	1.9×10^3	1.7×10^3	3.2×10^6	7	2	4	3	HIC	0.043	4.4×10^3	3.9×10^3	2.6×10^6	5	4	3	1	HIC		
0.052	2.7×10^3	2.1×10^3	1.4×10^6	5	3	3	1	HIC	0.048	7.1×10^3	6.0×10^3	4.0×10^6	5	5	3	1	HIC		
0.067	5.3×10^3	3.9×10^3	5.2×10^5	3	4	3	1	HIC	0.05	8.7×10^3	7.3×10^3	4.9×10^6	5	5	3	1	HIS		
0.074	8.6×10^3	6.1×10^3	8.1×10^5	3	5	3	1	HIC	0.052	9.3×10^3	9.8×10^3	1.3×10^6	3	4	4	2	HIC		
0.085	2.3×10^4	1.5×10^4	2.0×10^6	3	5	4	2	HIC	0.054	1.4×10^4	1.1×10^4	1.5×10^6	3	4	5	3	HIC		
									0.061	1.9×10^4	1.4×10^4	1.9×10^6	3	5	4	2	HIC		
									0.063	2.3×10^4	1.7×10^4	2.3×10^6	3	5	5	3	HIC		
On-off detector with post-selection																			
0.009	1.8×10^3				2	3	2	HIC	0.005	1.9×10^3				3	3	2	HIC		
0.012	3.6×10^3	3.9×10^3	2.1×10^9	45	2	4	2	HIC	0.008	2.3×10^3				3	3	1	HIS		
0.013	4.6×10^3	5.0×10^3	4.6×10^8	25	2	5	4	HIC	0.013	3.7×10^3	3.9×10^3	6.8×10^8	31	4	3	1	HIC		
0.022	1.0×10^4	1.0×10^4	1.1×10^9	27	3	3	1	HIC	0.014	4.4×10^3	4.6×10^3	9.0×10^7	15	3	4	2	HIS		
0.024	1.1×10^4	1.0×10^4	2.0×10^7	7	3	4	2	HIC	0.016	4.7×10^3	4.8×10^3	1.3×10^8	17	4	3	1	HIS		
0.035	3.1×10^4	2.6×10^4	1.7×10^7	5	4	4	2	HIS	0.02	6.0×10^3	6.0×10^3	7.6×10^7	13	5	3	1	HIC		
0.044	2.4×10^5	1.9×10^5	1.2×10^8	5	5	4	1	HIC	0.023	9.6×10^3	9.3×10^3	1.1×10^8	13	4	4	2	HIS		
									0.025	1.4×10^4	1.4×10^4	5.8×10^7	9	4	5	3	HIS		
									0.028	1.5×10^4	1.5×10^4	6.3×10^7	9	5	4	2	HIC		
									0.03	1.6×10^4	1.7×10^4	3.3×10^8	15	5	4	1	HIS		
									0.032	2.3×10^4	2.1×10^4	8.8×10^7	9	5	5	2	HIS		
Two-photon resolving detector without post-selection																			
0.009									0.005					3	3	2	HIC		
0.012									0.008					3	3	1	HIS		
0.013									0.013					31	4	3	1	HIC	
0.022									0.014					15	3	4	2	HIS	
0.024									0.016					17	4	3	1	HIS	
0.035									0.02					13	5	3	1	HIC	
0.044									0.023					13	4	4	2	HIS	
									0.025					9	4	5	3	HIS	
									0.028					9	5	4	2	HIC	
									0.03					15	5	4	1	HIS	
									0.032					9	5	5	2	HIS	

IX. ANALYSES OF OTHER KNOWN APPROACHES

In this section, we describe the methods and results of the analyses of the two other known approaches.

A. Approach using single-photon qubits with fusions assisted by ancillary photons

We first consider the approach using single photons for all qubits with fusions assisted by ancillary photons [5], which has been widely studied in the context of ballistic quantum computing [6–9]. In these previous works, non-RHG lattices are considered except for Ref. [8]; however, RHG lattices should be used to enable a solid error correction, as also mentioned in Refs. [6, 9]. Moreover, in these works, the detrimental effects of failed fusions corrupting nearby qubits are not treated comprehensively; instead, they regard a fusion failure as removing the corresponding edge and focus on finding percolation thresholds. Ref. [8] suggests a clever way to “purify” a large RHG lattice constructed by probabilistic fusions to a smaller lattice with faults below the threshold. However, the process is inherently not fault-tolerant and it is currently unclear how it affects the photon loss threshold.

Here, we consider an RHG lattice generated by the process shown in the main text, where every fusion is done by the scheme in Ref. [5]. We do not use the purification process in Ref. [8], which is worth investigating in future works. Under the noise model described in the main text, a fusion detects a loss with probability $1 - (1 - \eta)^2$, if losses in ancillary photons are neglected. Since a marginal state of every Bell state is maximally mixed, detection of a photon loss means complete loss of information; thus, $q_{\text{lett}} = q_{\text{sign}} = 1/2$ in such a case. If losses are not detected, the fusion fails with probability p_f , where the letter information of the Bell state still can be obtained [5]; namely, $q_{\text{lett}} = 0$ and $q_{\text{sign}} = 1/2$. These two cases make some central qubits deficient, which can be tracked using the methodology of analyzing nonideal fusions that is presented in the main text. HIC is used for the H -configuration to make the failure of a step-1 fusion affects only one central qubit; see Fig. 2 of the main text.

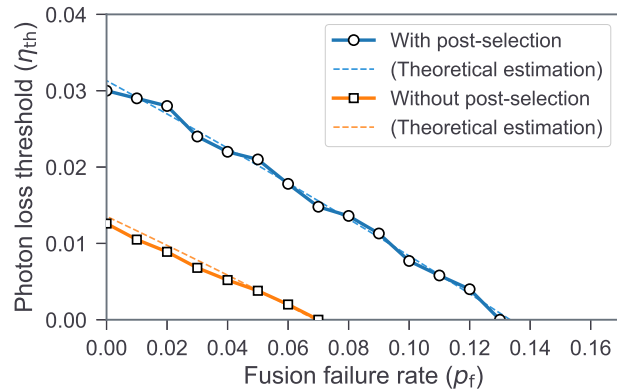


FIG. 14. Photon loss threshold η_{th} obtained from simulations or estimated theoretically as a function of the fusion failure rate p_f for the protocol using single-photon polarization qubits.

The photon loss thresholds calculated numerically by the method in Sec. VII are plotted in Fig. 14 with theoretical estimations for various values of p_f . The theoretical estimation is done by the following methods: We first assume that star clusters are not post-selected. For a central qubit q to be not deficient, the following conditions should be satisfied simultaneously:

1. Two step-1 fusions in the star cluster containing q succeed.
2. Four step-1 fusions in the four adjacent star clusters (one for each) do not detect losses.
3. Four step-2 fusions involved in the star cluster containing q do not detect losses. Two among them (that make q deficient if they fail) succeed.
4. q itself does not suffer a loss.

From above, we obtain the probability that a central qubit in the final lattice is intact: $p_{\text{int}}(\eta, p_f) = (1 - p_f)^4(1 - \eta)^{21}$. If star clusters are post-selected, the first and second conditions are no longer needed, thus we get $p_{\text{int}}(\eta, p_f) = (1 - p_f)^2(1 - \eta)^9$. Regarding a 50% chance of a Z -error as erasing the qubit by measuring it in the Z -basis (while ignoring the correlation of errors), a photon loss threshold η_{th} can be estimated by solving $1 - p_{\text{prc}} = p_{\text{int}}(\eta_{\text{th}}, p_f)$, where $p_{\text{prc}} = 0.249$ is the known cubic-lattice bond percolation threshold [10, 11].

Figure 14 shows that p_f should be less than about 10% (1%) even if η is only 1% when star clusters are (are not) post-selected. The failure rate of 10% can be achieved by using the BSM scheme of $N = 3$ in Ref. [5] where $p_f = 6.25\%$. For one BSM with $N = 3$, 32 photon-number resolving detectors (PNRDs) resolving up to 16 photons

and the ancillary states $|\Upsilon_1\rangle, |\Upsilon_2\rangle, |\Upsilon_3\rangle$ (two copies each) are required. $|\Upsilon_j\rangle$ is a 2^j -mode state defined as $|\Upsilon_j\rangle := |2, 0, 2, 0, \dots, 2, 0\rangle + |0, 2, 0, 2, \dots, 0, 2\rangle$. Although $|\Upsilon_1\rangle$ can be simply generated with two identical single photons and a beam splitter using Hong-Ou-Mandel effect [12], it is probably impossible to obtain $|\Upsilon_j\rangle$'s for $j \geq 2$ from single photons with linear optics [5]. Therefore, it is highly demanding to implement this MBQC protocol with linear optics due to the requirements of PNRDs that can resolve many photons and ancillary states hard to generate.

B. Approach using repetition codes

Now, we consider the approach using repetition codes, which is covered in our previous work [13]. In this protocol (called “MTQC”), side qubits are n -photon ones encoded in the basis of $\{|H\rangle^{\otimes n}, |V\rangle^{\otimes n}\}$, where n is a natural number. For central qubits, we first consider using m -photon qubits and then concatenate it with the N -repetition code. That is, we use the basis of $\left\{(|H\rangle^{\otimes m} \pm |V\rangle^{\otimes m})^{\otimes N}\right\}$ for the central qubits. In Ref. [13], the photon loss thresholds and resource overheads are analyzed in detail, but a rigorous analysis of the effects of nonideal fusions like that done for PTQC is lacking.

Since the n -photon encoding for side qubits is equal to the $(n, 1)$ parity-state encoding, the effects of nonideal fusions can be analyzed in the same way as done for PTQC with the $(n, 1)$ parity-state encoding. The difference between the two is the way that central qubits become deficient due to photon losses in themselves. In PTQC, central qubits are single photons, thus a central qubit becomes deficient with probability η . In MTQC, however, the deficiency rate due to photon losses in central qubits is $[1 - (1 - \eta)^m]^N$, which decreases exponentially as N increases. The photon loss thresholds recalculated based on these facts are presented in Fig. 15 with the previous values reported in Ref. [13], which shows that the recalculated photon loss thresholds are smaller than the reported values. In particular, it is observed that the central qubit encoding strategy does not improve the thresholds significantly. This discrepancy is because the detrimental effects of nonideal fusion affecting nearby qubits have not been sufficiently rigorously addressed.

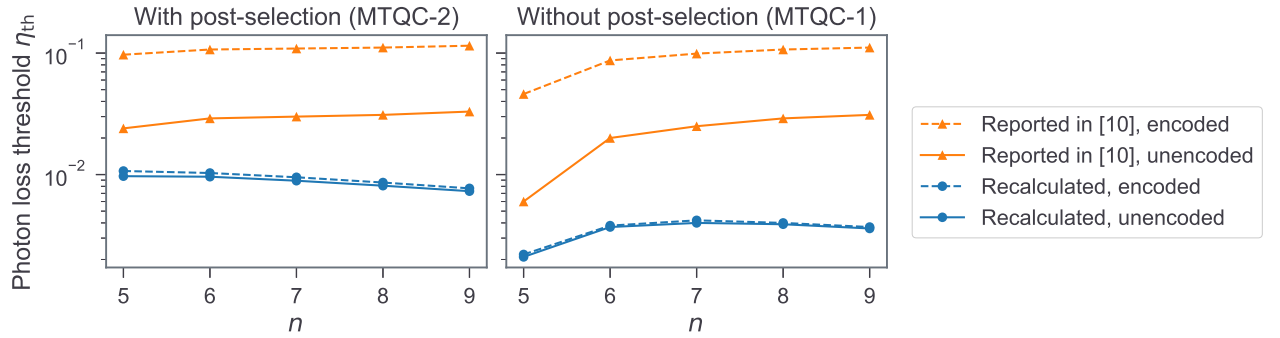


FIG. 15. Photon loss thresholds η_{th} as a function of n for MTQC, which are obtained from Ref. [13] and the recalculation using the methodology for analyzing nonideal fusions. Other parameters are $(m, N) = (2, 1)$ and $(m, N) = (2, 3)$ for the unencoded and encoded cases, respectively. Two subvariants of MTQC, one with the post-selection of star clusters and the other without it, are considered, which are respectively termed MTQC-2 and MTQC-1 in Ref. [13].

[1] S.-W. Lee, T. C. Ralph, and H. Jeong, Fundamental building block for all-optical scalable quantum networks, *Phys. Rev. A* **100**, 052303 (2019).

[2] N. Lütkenhaus, J. Calsamiglia, and K.-A. Suominen, Bell measurements for teleportation, *Phys. Rev. A* **59**, 3295 (1999).

[3] A. A. Hagberg, D. A. Schult, and P. J. Swart, Exploring network structure, dynamics, and function using NetworkX, in *Proceedings of the 7th Python in Science Conference*, edited by G. Varoquaux, T. Vaught, and J. Millman (Pasadena, CA USA, 2008) pp. 11 – 15.

[4] O. Higgott, Pymatching: A python package for decoding quantum codes with minimum-weight perfect matching, *ACM Trans. Quantum Comput.* 10.1145/3505637 (2021).

[5] F. Ewert and P. van Loock, 3/4-Efficient Bell measurement with passive linear optics and unentangled ancillae, *Phys. Rev. Lett.* **113**, 140403 (2014).

- [6] M. Gimeno-Segovia, P. Shadbolt, D. E. Browne, and T. Rudolph, From three-photon Greenberger-Horne-Zeilinger states to ballistic universal quantum computation, *Phys. Rev. Lett.* **115**, 020502 (2015).
- [7] H. A. Zaidi, C. Dawson, P. van Loock, and T. Rudolph, Near-deterministic creation of universal cluster states with probabilistic Bell measurements and three-qubit resource states, *Phys. Rev. A* **91**, 042301 (2015).
- [8] D. Herr, A. Paler, S. J. Devitt, and F. Nori, A local and scalable lattice renormalization method for ballistic quantum computation, *npj Quantum Information* **4**, 1 (2018).
- [9] M. Pant, D. Towsley, D. Englund, and S. Guha, Percolation thresholds for photonic quantum computing, *Nat. Commun.* **10**, 1 (2019).
- [10] S. D. Barrett and T. M. Stace, Fault tolerant quantum computation with very high threshold for loss errors, *Phys. Rev. Lett.* **105**, 200502 (2010).
- [11] C. D. Lorenz and R. M. Ziff, Precise determination of the bond percolation thresholds and finite-size scaling corrections for the sc, fcc, and bcc lattices, *Phys. Rev. E* **57**, 230 (1998).
- [12] C. K. Hong, Z. Y. Ou, and L. Mandel, Measurement of subpicosecond time intervals between two photons by interference, *Phys. Rev. Lett.* **59**, 2044 (1987).
- [13] S. Omkar, S.-H. Lee, Y. S. Teo, S.-W. Lee, and H. Jeong, All-photonic architecture for scalable quantum computing with greenberger-horne-zeilinger states, *PRX Quantum* **3**, 030309 (2022).